Remote Sensing Techniques for Surface Water Detection

by

Swastik Bimal Bhattacharya

B. Tech., Sardar Vallabhbhai National Institute of Technology, 2021

A thesis submitted to the

Faculty of the Graduate School of the

University of Colorado in partial fulfillment

of the requirements for the degree of

Master of Science

Department of Electrical, Computer and Energy Engineering

2023

Committee Members:

Y. T. Jade Morton, Chair

Prof. Yang Wang

Prof. Youjian (Eugene) Liu

Bhattacharya, Swastik Bimal (M.S. in Electrical Engineering)

Remote Sensing Techniques for Surface Water Detection

Thesis directed by Prof. Y. T. Jade Morton

In water resource management, environmental monitoring, and disaster response, surface water detection utilizing remote sensing is a crucial task as the measurement techniques provide important insights into their spatial distribution and dynamics. This thesis begins with a study of estimating hyperspectral measurements from multispectral acquisitions, which could in turn be used to differentiate between multiple land surface types including surface water. Through false color composites and examples of spectrum from land surfaces, spectral super-resolution using dictionary learning is demonstrated. With an Inverse Relative Deviation (IRD) of about 32dB spectral upsampling is performed on the study area used for training. Upon testing on a separate study area, the algorithm explored in the thesis is able to do so with an IRD of 20dB. The study also shows the distinct features in a reflected radiance spectrum that could help identify inland water bodies. Since these measurements have a very low repeat cycle, the dynamics of inland water bodies cannot be studied effectively. In this thesis, therefore, the use of GNSS-R measurements along with optical remote sensing data are discussed to detect surface water bodies and identify windows of continuous samples over water. GNSS as a signal of opportunity is discussed. These measurements along with optical indicator NDVI are used to segregate reflections of GNSS tracks over water. With a true positive rate of approximately 70%, reflections from water bodies and land can be segregated. It is observed that carrier phase measurements alone cannot be used for segregation of reflections over water as they are intermittently straddling over land and water. Thus a window of coherency detection will have reflections over both land and water, thereby necessitating the use of GNSS-R along with optical measurements. After classification, windows with consecutive reflections over water are extracted and their distribution is determined for over a month, where more than 50% of the windows had a circular length of 0.97, showing highly coherent reflections.

Dedication

To Maa and Baba.

Acknowledgements

I want to express my gratitude to my advisor, Prof. Jade Morton, for her constant support in helping me complete my project successfully. She has provided me with excellent knowledge and experiences as I have moved toward this path with her patience, inspiration, passion, and amazing skill in the subject. Without her help, writing a Masters thesis would have been a completely different experience. Prof. Yang Wang and Prof. Youjian Liu have my heartfelt gratitude for giving me the chance and the setting to work on such high-tech projects. Also, I would like to express my gratitude for the assistance I received from Dr. Bruce Kindel, Dr. Gongguo Tang, Mr. Kedar Remane and Mr. Jatin Chaudhary in introducing, studying, and putting into practice the strategies necessary to achieve the objective of my thesis. I also want to thank my parents and my coworkers for their never-ending support, encouragement, and inspiration as I worked to finish this thesis. The completion of this thesis was made possible by the efforts of numerous persons, for whom I sincerely express my gratitude.

Contents

Chapter

Figures

Figure

Chapter 1

Introduction

This thesis focuses on remote sensing of surface water using optical and radio signals. Using the optical and reflected microwave signal measurements, the thesis attempts to detect inland water bodies. Optical remote sensing involves a system of airborne or spaceborne sensors that acquire images of an observed area across visible and infrared bands of the electromagnetic spectrum. Due to the different materials comprising a particular land surface, the reflectivity of the surface is different at a wavelength. This gives rise to the distinctive reflected radiances based on the different land surface types. This characteristic is exploited for land use classification. However, in cases where measurements are required at very short wavelength intervals (for example, 10nm intervals), specialized instruments are required that can capture the reflections from an observed area across wavelengths separated by small intervals. This is called hyperspectral remote sensing. One of the prime challenges for the deployment of such instruments on spaceborne missions is the complexity and weight of the instrument. To address this issue, this thesis demonstrates a study that estimates hyperspectral measurements from narrow-band multispectral acquisitions using dictionary learning and random forests.

Optical measurements are an effective way of identifying surface water due to the difference in the reflected radiance in the Near Infra-Red (NIR) and red bands as compared to those over land. However, some of the water bodies can be narrow, such as rivers. Optical images from spaceborne payloads on board the Sentinel-2 satellites provide images at 20m resolution every 10 days. Due to the lower temporal resolution of high spatial resolution images, it is difficult to monitor the extent

and dynamics of inland water bodies daily. To address this, there have been developments toward using reflected GNSS signals to identify inland water bodies. This thesis uses GNSS measurements along with optical and Synthetic Aperture Radar (SAR) backscatter measurements to identify water bodies along a GNSS reflection track.

Surface water resources are an important part of the ecology of the Earth and provide both people and wildlife with necessary services. These resources are used for many different things, such as irrigation, industrial processes, recreation, and drinking water. The availability and quality of surface water resources are continually shifting, necessitating careful monitoring and resource management. This thesis consists of an adaptation of works in [11][13][12] divided into different chapters to demonstrate the different features that the data products show towards remote sensing over inland water. This thesis is organized into six chapters that deal primarily with detecting inland water bodies using GNSS and Optical Remote Sensing measurements.

(1) Chapter 1 has a brief introduction to the studies done in the thesis and its organization.
(2) Chapter 2 introduces optical remote sensing and indicator that could be used to characterize different land surface types.
(3) Chapter 3 is an adaptation of [11] where spectral super resolution is discussed and extends the application to surface water detection by explaining the difference in the optical spectrum.
(4) Chapter 4 introduces GNSS as a signal of opportunity, discussing how it can be used as a system to ascertain land surface properties.
(5) Chapter 5 is an adaptation of works in [13][12] to detect surface water using GNSS-R along with optical and SAR measurements and corroborate them with coherency detection using carrier phase measurements.
(6) Chapter 6 discusses the conclusions and future scope of the studies in this thesis.
(7) Appendix A briefly explains the K-SVD algorithm to train an overcomplete dictionary.
(8) Appendix B explains the procedure to detect coherency in a window of reflection.

Chapter 2

Optical Remote Sensing and Land Surface Indicators

Optical remote sensing is a technique that uses sensors to record electromagnetic radiation in the visible, near-infrared, and short-wave infrared ranges to learn more about the Earth's surface. This technology has many applications in agriculture, forestry, land-use management, and other fields. On a variety of platforms, including satellites, aircraft, drones, and ground-based devices, optical remote sensing systems can be used. These systems gather data, which is then utilized to produce images, maps, and other outputs that academics and decision-makers may examine and comprehend.

2.1 Optical Image Acquisition

The procedure of taking and compiling photographs of the Earth's surface using optical sensors is referred to as optical remote sensing image acquisition. This procedure includes several processes, including choosing the right sensor, deploying the sensor, gathering data, processing the data, and analyzing the images that are produced.

(1) **Selection of Sensor:** The right sensor must be chosen for the particular application before beginning the optical remote sensing image acquisition process. The spectral bands of the sensor, the coverage area, the spatial resolution, and the temporal resolution are all important factors to take into account. For instance, it could be necessary to use a sensor with a high spatial resolution to record specifics about the land cover and a sensor with a huge coverage area to keep track of significant environmental changes. For example, images

provided by Landsat-8 OLI/TIRS instruments are at a 30m spectral resolution, which is helpful to identify water bodies such as river, or in urban applications. Instruments such as the MODIS provide images at 1km resolution which could not be used in the aforementioned applications, but can be used in areas that deal with observing larger areas such as agricultural fields.

(2) **Deploying the Sensor:** The chosen sensor must be deployed in the proper manner and place after being chosen. Depending on the intended coverage area and spatial resolution, this may entail mounting the sensor on a satellite, airplane, drone, or ground-based platform. To guarantee that the data gathered is precise and dependable, the sensor must also be correctly calibrated [68]. Some examples of these include the Airborne Visible and Infra-Red Imaging Spectrometer (AVIRIS) which is on an airborne platform providing spatial resolution of approximately 11m, or the Sentinel satellites that are spaceborne missions covering a larger area in a single track with a spatial resolution of approximately 20m.

(3) **Data Collection:** Data gathering can start once the sensor has been deployed. This is done by capturing images of the earth's surface across all the optical wavelength bands the selected sensor provides. The photos are typically taken in digital format and can either be stored on the sensor itself or sent for processing to a ground station.

(4) **Process and Analysis:** To extract data about the Earth's surface, this involves turning the raw image data into a format that may be used, such as a georeferenced image. This could involve, among other things, picture augmentation, image categorization, and data fusion approaches.

Certain factors need to be taken into consideration when developing an optical remote sensing system:

(1) **Spatial Resolution:** Spatial Resolution refers to the minimum distance between two observations that could be discerned with high accuracy. It is commonly measured in meters and depends on the size of the pixels in the image. The required spatial resolution

will vary depending on the application, with applications like land cover mapping and urban planning requiring higher spatial resolution.

(2) **Spectral Resolution:** The quantity and width of the spectral bands that the sensor can capture are referred to as spectral resolution. This may affect one's capacity to recognize features like water quality and mineral deposits as well as distinguish between various types of plants and land cover.

(3) **Temporal Resolution:** The amount of time that images are recorded across a specific area is referred to as the temporal resolution. This may affect our capacity to track long-term changes, such as shifts in the topography brought on by calamities or human activity.

(4) **Quantization Level or Radiometric Resolution:** It is the number of bits or quantization levels that are used to generate the data product to accurately describe the measurements taken by the sensor. It forms a part of the sensor specification.

(5) **Coverage Area:** The sensor's coverage area will vary depending on the platform's altitude when taking pictures. While lower altitude platforms like drones may collect photographs at higher spatial resolutions over smaller areas, higher altitude platforms like satellites can record images over wider areas.

2.2 Emission Spectra

The radiation released by the Earth's surface at various wavelengths is referred to as the emission spectra from various land surfaces, and it can be used to distinguish and classify various forms of land cover [74]. Depending on the temperature, emissivity, and reflectance characteristics of the surface, various land surfaces emit radiation in various portions of the electromagnetic spectrum. These characteristics are controlled by variables like surface temperature, vegetation cover, and soil moisture content [37].

For instance, the type of vegetation, its density, and its moisture content all affect the emission

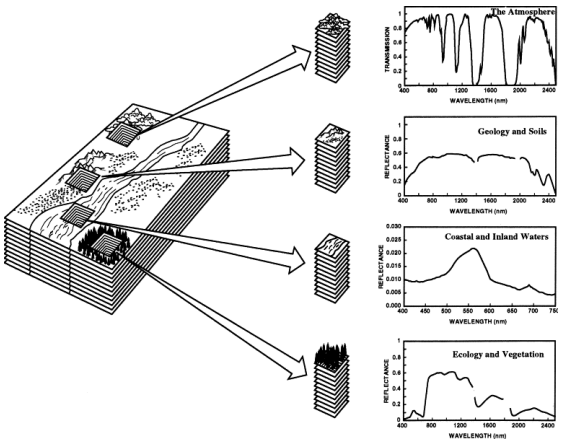

Figure 2.1: A concept of imaging spectroscopy to characterize reflections over each pixel. As seen, depending on the land surface type, the reflectances differ, which contribute to different spectra for different land surface type. [37]

spectrum that is characteristic of that particular type of plant. Stressed or diseased vegetation may have altered reflectance characteristics, typically having a higher reflectance in the near-infrared region of the spectrum and a lower reflectance in the visible region [67] Similarly, different soil and rock kinds can be distinguished by their varied emission spectra [39]. For instance, rocky surfaces may have higher emissivities in the shorter-wavelength visible and near-infrared areas of the spectrum than bare soil, which normally has a high emissivity in the mid-infrared part of the spectrum and a lower emissivity in those regions.

Depending on variables like water temperature, depth, and turbidity, water bodies also produce radiation in various areas of the electromagnetic spectrum [77]. While turbid or murky water may have higher emissivities in the mid-infrared part of the spectrum due to the presence of suspended particles, clear water typically has a low emissivity in the mid-infrared part of the spectrum and a higher emissivity in the visible and near-infrared parts of the spectrum. Fig. 2.1 shows the effects that solar radiance has to go through when it is passing through the atmosphere and reflection from a surface which forms the basis of optical remote sensing applications.

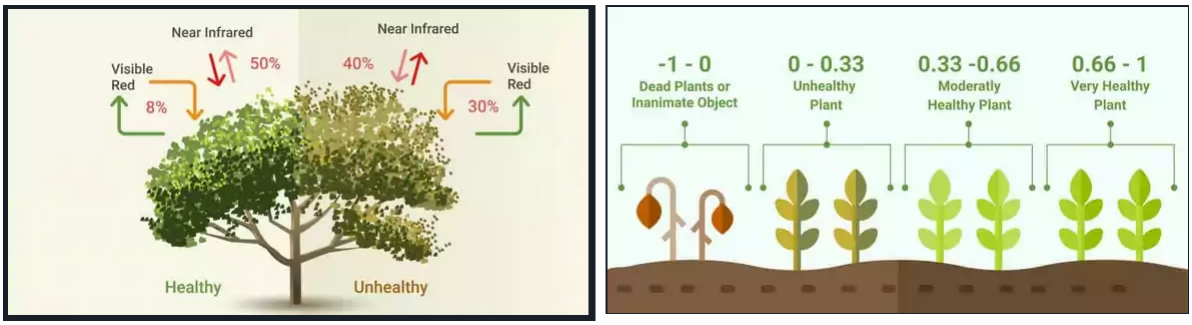

Figure 2.2: The different proportions of NIR and red band reflections from plants that can be used to study their health or type [3].

2.3 Normalized Difference Vegetation Index

Calculating the Normalized Difference Vegetation Index (NDVI) is a crucial use of optical remote sensing. NDVI is computed using reflected radiance signal from airborne platforms or remote sensing satellites [67]. The index calculates the relative level of photosynthetic activity in vegetation and gives a numerical assessment of the condition of the plant. The NDVI is calculated using the following formula:

$$NDVI = \frac{R_{NIR} - R_{RED}}{R_{NIR} + R_{RED}} \tag{2.1}$$

Here, R_{NIR} is the surface reflectance in the NIR band, and R_{RED} is the surface reflectance in the red band. The range of NDVI values is from -1 to +1, with negative values denoting non-vegetated places like water or bare ground and positive values denoting robust vegetation. The vegetation is healthier when the NDVI value is higher. When the NDVI is 0, there is no vegetation present. NDVI can be used to track long-term changes in vegetation, such as variations in the quantity of cover or alterations in the health of the plant [83]. Applications for this data include crop health monitoring, evaluating the effects of natural disasters, and managing natural resources. Fig. 2.2 shows the behavior of NIR and red band reflections over different plants that can be useful in characterizing them.

The NDVI has the drawback of only being sensitive to changes in the quantity of vegetation

vigor and not to changes in the structure or composition of the plant. For instance, NDVI could not be responsive to changes in vegetation height or density. Other vegetation indices might be more suited in certain circumstances. Another drawback of NDVI is that it could not be accurate in areas with mixed vegetation, locations with high concentrations of atmospheric aerosols, or areas with high concentrations of water vapor. Other vegetation indices or adjustment techniques might be required in these circumstances. Despite these drawbacks, NDVI is still a popular vegetation index and a useful tool for tracking changes in the health of vegetation. Decision-makers in a range of disciplines can use the information supplied by NDVI to make well-informed choices on resource management and land use.

2.4 Application

Agriculture is a crucial area for optical remote sensing applications. Crop health can be tracked via optical remote sensing, which can also be used to calculate yields and plan irrigation and fertilizer applications. Farmers and agronomists can spot parts of the field that could require extra inputs or attention, including those impacted by disease or pests, by examining photographs of crops taken over time. Forestry management is a crucial area where optical remote sensing can be used. Researchers can determine the quantity and grade of timber, locate pest- or disease-affected areas, and track changes in forest cover over time by examining photographs of forests.

Land-use management practices like urban planning [52] and resource management also employ optical remote sensing. Researchers can calculate population density, pinpoint regions with heavy traffic or pollution [65], and track changes in urban land cover over time by examining pictures of urban areas [18]. Optical remote sensing can be used in natural resource management to track the spread of invasive species, track changes in water supplies [53], and track changes in land cover brought on by human activity or other natural processes like wildfires [6] or erosion.

There are many methods for analyzing data from optical remote sensing, including image processing, machine learning, and data fusion. Images are improved and analyzed using image processing techniques, such as by removing noise or highlighting important elements. To categorize

and detect features in photos, such as different types of crops or land cover, machine learning techniques are applied. To develop more thorough maps and images, data fusion techniques are used to merge data from many sources, such as merging optical remote sensing data with data from other sensors, such as radar or LiDAR.

The necessity to take atmospheric factors into account, such as the scattering and absorption of radiation by aerosols and gases, is a challenge when employing optical remote sensing. The signal that the sensors receive as a result of these impacts may be distorted or weakened, resulting in data inaccuracies. Researchers utilize atmospheric correction methods, such as the use of ground-based data or the use of atmospheric models, to account for these impacts. Dealing with variations in surface reflectance, such as differences in the amount and kind of vegetation or fluctuations in the presence of water or soil, is another difficulty in using optical remote sensing. Researchers employ methods like normalization, which entails dividing the reflectance values by a reference value to get a more uniform metric, to overcome these variations.

Apart from the need to make atmospheric corrections, the complexity increases when an application requires acquisitions over multiple wavelengths separated by short intervals (hyperspectral measurements). Such applications include crop classification, soil health monitoring, and disease detection. Most of these hyperspectral instruments use a push-broom or a whisk-broom arrangement to make continuous acquisitions over multiple wavelengths. To develop such instruments for space-borne missions, it is necessary to reduce some of the complexity of the instrument so that they become economically viable. Therefore, studies on algorithms that can estimate hyperspectral measurements from multispectral acquisitions are necessary. The next chapter discusses the work in [11] where dictionary learning is used to demonstrate spectral super-resolution over images acquired by the Airborne Visible and Infra-Red Imaging Spectrometer (AVIRIS) to address the above challenge.

Chapter 3

Hyperspectral Remote Sensing and Estimation of Intermediate Bands from Multispectral Data

The hyperspectral sensors collect data on hundreds of small and continuous bands throughout the electromagnetic (EM) spectrum to determine the reflected radiance spectrum. They do so over the visible (380-1000nm) and infrared (1000-2500nm) regions of this electromagnetic spectrum using instruments like the Aerial Visible and Infra-Red Imaging Spectrometer (AVIRIS). These instruments generate data in the form of an image data cube, with each channel made up of images taken at various center wavelengths. To map grassland, forests, water, plants, and clouds, for example, not all of the spectral channels of such a spectrometer are necessary [14]. There are specific applications where hyperspectral data are crucial for scientific research, particularly to assess material abundance, illness detection, air, and water quality monitoring, etc. In these circumstances, retrieving hyperspectral data is made easier and more practical by spectral super-resolution from multi-spectral bands.

Studies done by Boardman and Green et al. [14]; Townsend et al. [80], Ustin et al. [82], Lee et al. [56] and Thompson et al. [78], for example, have made crucial contributions to the development of hyperspectral imaging and applications in earth observation. The acquisitions are made by an imaging spectrometer which has a push-broom or a whisk-broom arrangement, which requires continuous translation and switching actions to cover a swath of the earth's surface from an altitude. To capture reflected radiances with a high spatial and spectral resolution, the acquisition methodology becomes complex and has a possibility of high noise and low repeat cycle, thereby not

feasible for capturing dynamic features of the surface. Therefore, spectral super-resolution from multispectral acquisitions is being worked upon by several research groups as they provide an option to execute compressed sensing at high spatial resolution with a high repeat cycle. Galliani et al. [26] implemented a 2-dimensional Convolutional Neural Network (CNN) to estimate hyperspectral images from RGB acquisitions, with an SNR of approximately 21dB. Arad et al. [7] explain the sparse nature of hyperspectral images with the help of metamerism, which in turn provides an explanation of the usefulness of dictionary learning for spectral super-resolution. Aeschbacher et al. [4] proposed an algorithm based on [79] that outperformed [26]. These algorithms are meant for hyperspectral image reconstruction from RGB acquisitions from a stationary camera, and not an airborne or spaceborne sensor. They also describe their application in airborne and spaceborne acquisitions, with their efficacy around 7-9% RMSE. The NTIRE 2018 challenge on Spectral Reconstruction from RGB Images [8] also evaluates several works in this domain. An algorithm involving an optimized input layer for selecting appropriate multispectral bands for a fully connected deep neural network with 1-D convolutional layers and residual layers by Gewali et al. [30] has a similar premise. The methodology for spectral super-resolution described in this chapter has the following objectives:

- Reconstruction of hyperspectral signal from narrow equally-spaced multi-spectral bands using dictionary learning algorithm of K-Singular Value Decomposition (K-SVD) [5].
- Improving the reconstructed signal after dictionary learning using Random Forest (RF) Regression [15].
- Comparing the improved reconstruction post RF Regression with the actual hyperspectral signal.
- Evaluate the algorithm over different scenes.

3.1 Study area and dataset

For this study, acquisitions from the airborne campaign of Airborne Visible and InfraRed Imaging Spectrometer (AVIRIS) conducted over the United States are used. Data is captured over

Figure 3.1: Location of the AVIRIS flight and study area.

several strips as part of the campaign. The dataset is first orthorectified and then used for the study.

3.1.1 Study Area

The orthorectified image tile used for this study is acquired over the region of Monterey Bay, California, USA. The rectangular bounds of the image tile have the coordinates 36.545^{o}N 122.107^{o}W, 36.544^{o}N 122.007^{o}W, 37.065^{o}N 122.000^{o}W, and 37.066^{o}N 122.101^{o}W. This study area comprises different land features such as vegetation, urban canopy, water, and clouds. They have different spectra due to their different emission characteristics across visible and infrared bands. The image used for the study was acquired on October 29, 2008, at 20:15 UTC (12:15 Local Time). The pixel size of image acquisition is 11.5m. The location of the study area is shown in Fig. 3.1.

3.1.2 AVIRIS Spectra

AVIRIS uses 224 detectors with a spectral bandwidth of 10 nm to sense in the EM range of 380 nm to 2500 nm [14]. For each scan, the equipment uses 224 detectors and a system of scanning

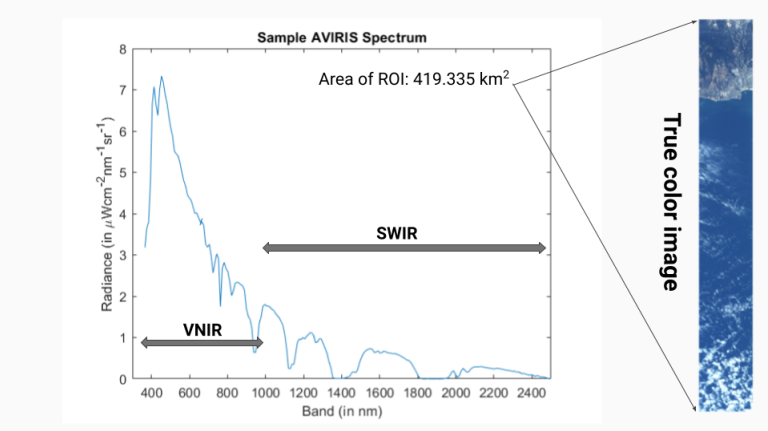

Figure 3.2: Sample AVIRIS spectrum over land, and the true color image of the studied area.

mirrors that are whisked back and forth to collect 677 pixels [14]. The radiance spectrum measured by AVIRIS is made up of the solar irradiance at the top of the atmosphere, atmospheric scattering and absorption, and surface spectral reflectance. An example spectrum over land, with the true color image of the image tile, is shown in Fig. 3.2.

3.1.3 Sparsity of hyperspectral data

The estimation of hyperspectral from multispectral measurements is an ill-posed problem due to the higher dimensional hyperspectral data. It is unlikely that a multispectral instrument could perform the inverse of this many-to-one mapping. As mentioned in [7], the sparsity of emission spectra can be explained by the phenomenon of metamerism [64], where light exhibits the same response from a sensory system. Depending on the sensed spectral segment, they have a different power distribution. The material composition and illumination dictate the spectral reflectance of an object, which could be generally viewed as a linear sum of the reflection spectra of different materials in the object [58]. It can be assumed that only some of the materials have the maximum contribution to the overall spectrum. Therefore, multispectral images are a sparse combination of the basis spectra stored in a dictionary [7].

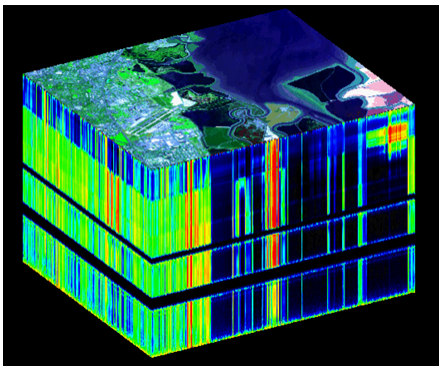

Figure 3.3: A sample of the AVIRIS datacube.

3.2 Methodology

3.2.1 Data pre-processing

Fig. 3.3 shows a portion of the AVIRIS acquisition in the form of a data cube. In this study, the data cube is of the size 4800x660x224. In this case, 224 is the number of bands in which the measurements have been taken. This data cube is reshaped to a matrix of 3,168,000 rows and 224 columns, such that each row resembles a row vector of dimension 224. Each row vector is the spectrum at each pixel of the AVIRIS tile. Out of them, 70% of the row vectors are taken as the training set, 20% as the validation set, and 10% as the testing set. The data cube is reshaped so that the K-SVD algorithm can be used.

3.2.2 K-Singular Value Decomposition

The ill-posed problem of estimating the hyperspectral measurements is attempted by training an overcomplete dictionary. This is done using K-Singular Value Decomposition (K-SVD) [5] algorithm. The algorithm has a flexible nature, where it alternates between sparse coding and dictionary update stages. For super-resolution, the dictionary is first sub-sampled to the dimension of the input data. The down-sampled dictionary is used to calculate the transform coefficients that are, in turn, used with the original dictionary to reconstruct the hyperspectral signal.

The dictionary to be trained is of the form:

$$\Phi^* = \begin{bmatrix} \Phi_1 & \Phi_2 & . & . & \Phi_i & . & . & \Phi_P \end{bmatrix} \tag{3.1}$$

Here, each of the Φ_i is an N-dimensional column vector, and P is the number of atoms in the dictionary. The value of P has to be greater than N for K-SVD. Along with this, the training, validation, and testing data are for the following form:

$$f = \begin{bmatrix} f_1 & f_2 & . & . & f_i & . & . & f_L \end{bmatrix} \tag{3.2}$$

In Equation 3.2, each of the f_i is an N-dimensional column vector, denoting the AVIRIS spectrum at each pixel. Here, L is the number of samples. Now, the training data and the initial dictionary are put through the K-SVD process as outlined in [5].

3.2.3 Random Forest regression

Random Forest (RF) algorithm was developed by Breiman et al. [15]. It is a classifier that consists of a collection of tree classifiers $\{h(\mathbf{x}, \Theta_k), k = 1, ...\}$ where the Θ_k that are independent identically distributed (i.i.d) random vectors and each tree casts a unit vote for the most popular class at input $\mathbf{x}$. In the case of a regression problem, the RF is created by growing the trees depending on a random vector, where the tree estimator h($\mathbf{x}$,Θ) takes on numerical values and not a class label. The output is numerical and the training set is assumed to be independently drawn from the distribution of the random vector Y, $\mathbf{X}$. The mean-squared generalization error for any numerical predictor $h(\mathbf{x})$ is:

$$E_{\mathbf{X},Y}(Y - h(\mathbf{x}))^2 \tag{3.3}$$

Initially, for the experimentation, the input row vectors are down-sampled to a lower dimension consisting of measurements of equally spaced bands. The number of bands is tuned to different values to reach an optimum number of bands. As per this, the K-SVD algorithm is used to train a dictionary with 448 atoms. This dictionary is trained for different sparsity levels using Orthogonal Matching Pursuit (OMP) [81]. Post the super-resolution operation in Section 3.2.2, to improve the

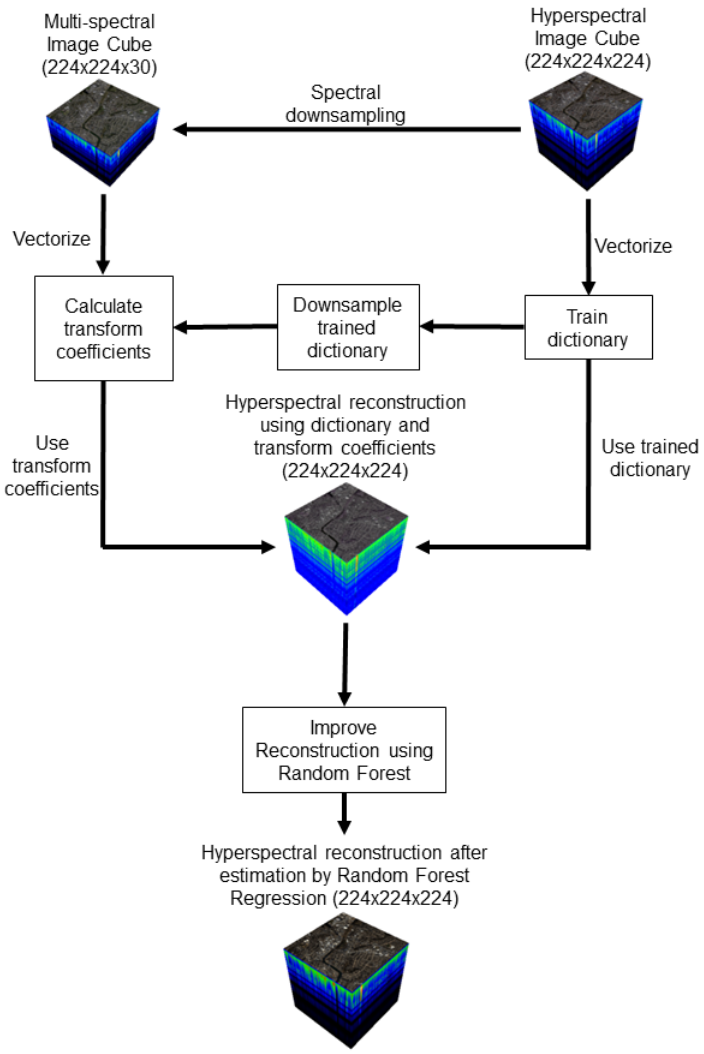

Figure 3.4: Process of hyperspectral image reconstruction from multi-spectral bands

output, the results are fed into an RF regressor to get an improved reconstructed spectrum. The reconstruction operation is shown in Fig. 3.4.

3.3 Model training

The quality of reconstruction is assessed using a metric called Inverse Relative Deviation (IRD) for each band, which is calculated in Decibels (dB) is defined as:

$$IRD_i = 10log_{10}(\frac{||f_i||_2^2}{||f_i - \hat{f}_i||_2^2}) \tag{3.4}$$

In Equation 3.4, f_i is the column vector of actual AVIRIS acquisition for a wavelength band i, while $\hat{f}_i$ is the column vector of the reconstructed samples for a wavelength band i. The overall IRD across all bands can be defined by:

$$IRD = 10log_{10}(\frac{||f||_2^2}{||f - \hat{f}||_2^2}) \tag{3.5}$$

In Equation 3.5, f forms the matrix by consisting of column vectors f_i and $\hat{f}$ is the matrix with column vectors $\hat{f}_i$, where $i = 1, 2, ..., 224$.

To reach an optimum level of sparsity for the row vectors, dictionaries were trained for different sparsity levels using OMP [81]. It is found that when the maximum sparsity is set to 30, the error in reconstruction is minimal and the time to train is less as compared to an increased number of non-zero transform coefficients for an atom. Also, the reconstruction process described in Section 3.2.2 is applied to different levels of downsampling. As can be seen, the highest reconstruction IRD on the training set can be obtained when the number of input bands is 30 as per Fig. 3.5. Therefore, for training the model, the number of input bands is set to 30, and the maximum sparsity is set to 30. The K-SVD algorithm is run for 10 iterations. The trained dictionary is downsampled by the method used to decimate the hyperspectral input data. The transform coefficients are calculated from the decimated dictionary, which is then used with the original dictionary to estimate the hyperspectral reflected radiances.

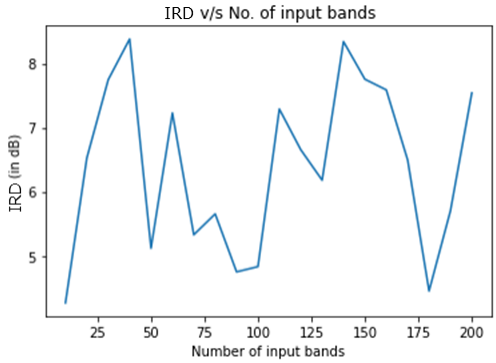

Figure 3.5: IRD of reconstruction v/s number of input bands in reconstruction for Sparsity=30

After the measurements are reconstructed using K-SVD, the samples are passed through an RF regressor made up of 10 tree estimators. Random Forest has been chosen for reconstruction post K-SVD since it is observed that the measurements across the bands are not correlated to each other. Therefore attempts towards improving reconstruction would be effective if a random tree estimator is chosen as it can estimate any missing value in reconstruction. It is also impervious to overfitting. This is the model training process that is depicted in Fig. 3.4.

3.4 Evaluation of spectrum and image reconstruction

Dictionaries are trained for different sparsity levels between 10 and 200, with an increment of 10. As mentioned earlier, it is observed that a minimum of 30 non-zero coefficients are required to reconstruct the signals, in the sparse-coding stage using OMP. With the number of equally spaced input bands set to 30 for the reconstruction process, it is observed that the reconstruction output can trace the general trend of the original spectrum. This is more evident when the reconstructed spectrum is scaled by a factor of 0.134 (dividing sparsity=30 by the total number of bands=224) even though it is noisy. This is also seen in Fig. 3.6. In Fig. 3.7, the reconstructed output after estimation using an RF regressor is shown. As it is observed, the reconstructed spectrum is similar to the captured measurements.

The spectrum for the mean absolute error and the ratio of reconstruction to the native radiance is derived and shown in Fig. 3.8 and Fig. 3.9 respectively. It can be deduced that the mean

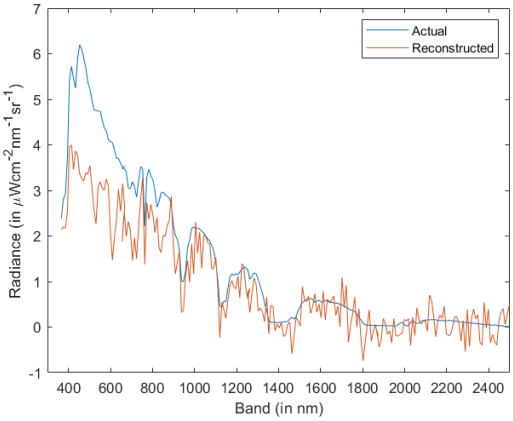

Figure 3.6: Example of reconstructed and actual radiance spectrum from dictionary trained with sparsity=30 and with 30 input multi-spectral bands over urban canopy

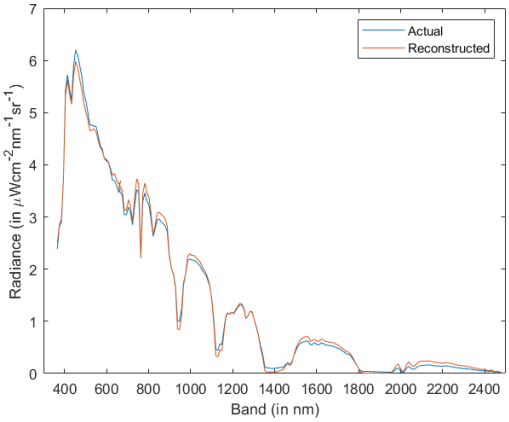

Figure 3.7: Example of reconstructed and actual radiance spectrum after estimation using Random Forest Regression over urban canopy

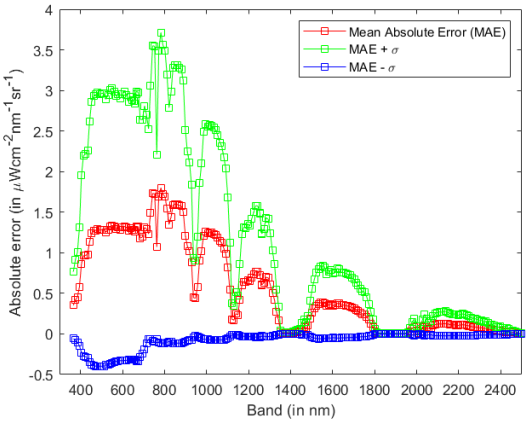

Figure 3.8: Spectrum for absolute error in reconstruction across study area

absolute error and the standard deviation are small when compared to the actual radiance at that wavelength. However, for increasing wavelength, the ratio of reconstructed to actual measurement increases. In the visible region, this ratio remains near 1, depicting a high quality of reconstruction.

On the testing set, Fig. 3.10 displays the IRD for the reconstruction of each band across all pixels before (after dictionary learning) and after improving reconstruction using the RF regressor. Reconstruction is observed to have undergone a substantial improvement. On the testing set, the total reconstruction IRD is estimated to be 31.58dB.

3.5 Discussions

In this study, it has been found that using an overcomplete dictionary alone to reconstruct signals will not result in a good reconstruction in terms of IRD, with the maximum and minimum values for all bands being 20dB and -40dB, respectively. However, it has been found that estimation using RF regression yields an overall IRD of 31.58dB, a maximum IRD of more than 35dB, and a minimum of roughly 3dB across all bands. The drop in IRD seen for bands with centers at 1400 nm and 1900 nm is linked to a high absorption from atmospheric water vapor. Such reconstructions open the door to using machine learning and sparsity-based algorithms to develop techniques for reconstructing hyperspectral images from a small number of narrow multi-spectral bands. However,

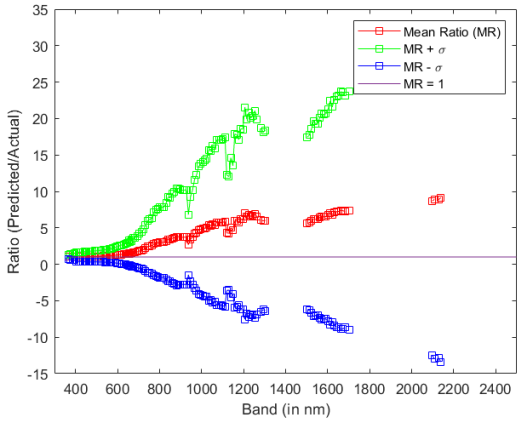

Figure 3.9: Spectrum for the ratio of radiance after reconstruction to actual AVIRIS spectra across study area

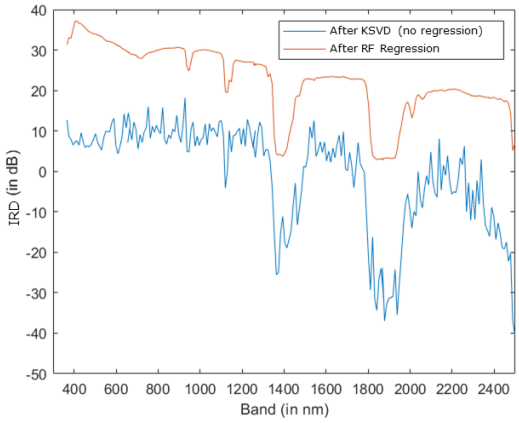

Figure 3.10: IRD of reconstructing each band before and after RF regression

to assess the durability and adaptability of this method under a variety of land surface types and atmospheric circumstances, such methods need to be evaluated over a wide range of targets and areas utilizing numerous sets of AVIRIS data. Therefore, in an attempt to verify the applicability of the model for a region with similar surface characteristics, the model is implemented on a tile over the cities of Los Angeles, California, and Boulder, Colorado. Fig. 3.11 shows a comparison of the original true color acquisition with a reconstructed true color image over Los Angeles. It is also seen that the reconstruction IRD after RF regression reduces to a maximum of about 20dB and a minimum of about -10 dB. A similar effect is seen when the model is used over Boulder, CO. A possible explanation for this could be the effect of a consistently increasing elevation. An elevation-based correction might improve the reconstruction in such cases.

This exercise has led to the analysis of AVIRIS spectra from different land surface types. It is observed that over water, there is a lower magnitude of emission in the infrared region than over land. An example of this is shown in Fig. 3.12. Since NDVI is the ratio of the difference between NIR and Red reflected radiance to the sum of NIR and red reflected radiance, it can be understood that for negative NDVI, the target surface is a water body. However, an increase in turbidity can lead to higher NIR emissions, leading to higher NDVI. Fig. 3.13 shows the false-color composite, showing the distinct land surface features that can help segregate into different land surface types. These acquisitions are however have a very low repeat cycle. This makes it difficult to use optical remote sensing datasets to study the inland water body dynamics daily. Latest developments in using GNSS as signals of opportunity have made it possible to track simultaneously multiple reflections from the earth's surface separated by approximately 100km. This, along with optical acquisitions can be used to study inland water bodies daily, which is discussed in subsequent chapters.

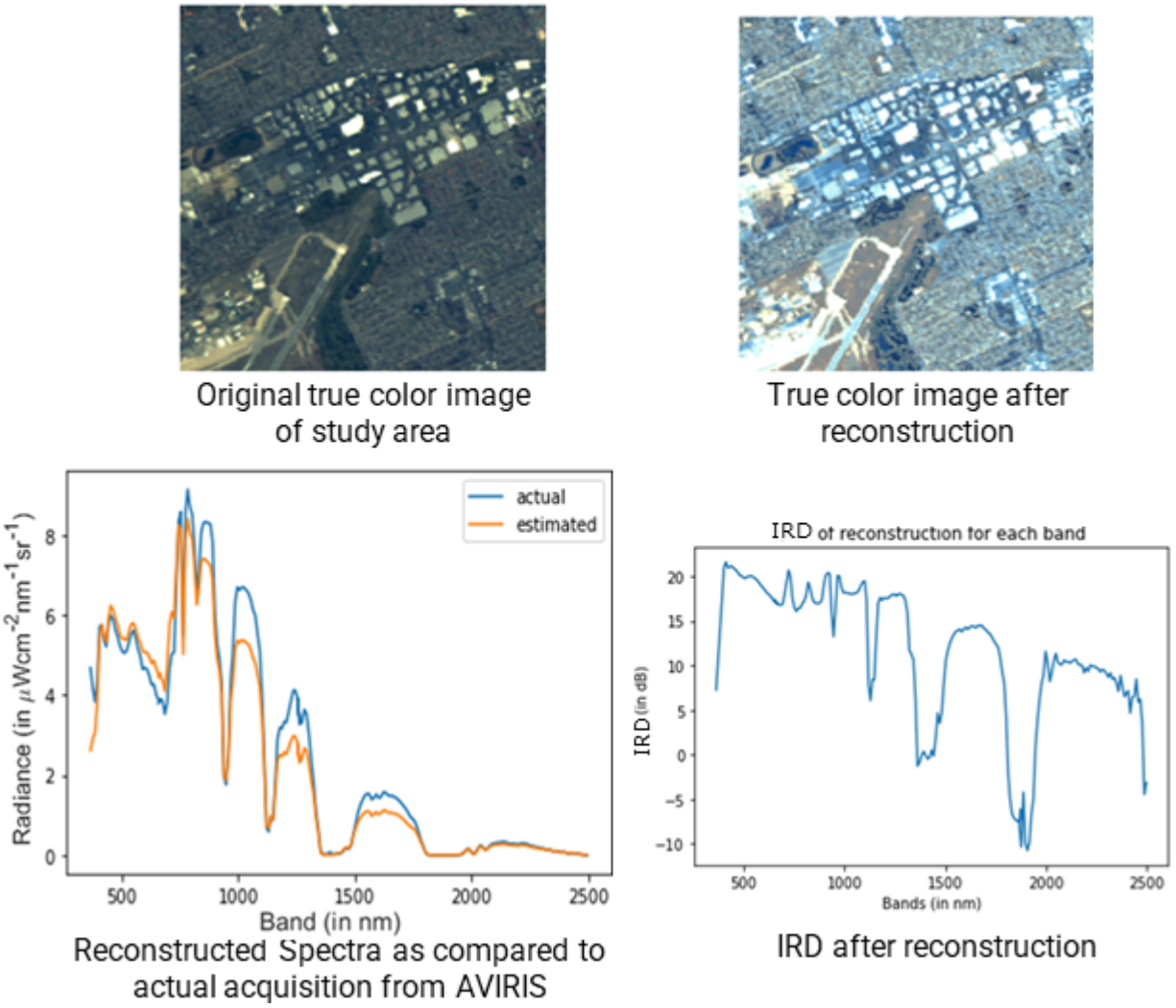

Figure 3.11: Reconstruction over Los Angeles, CA

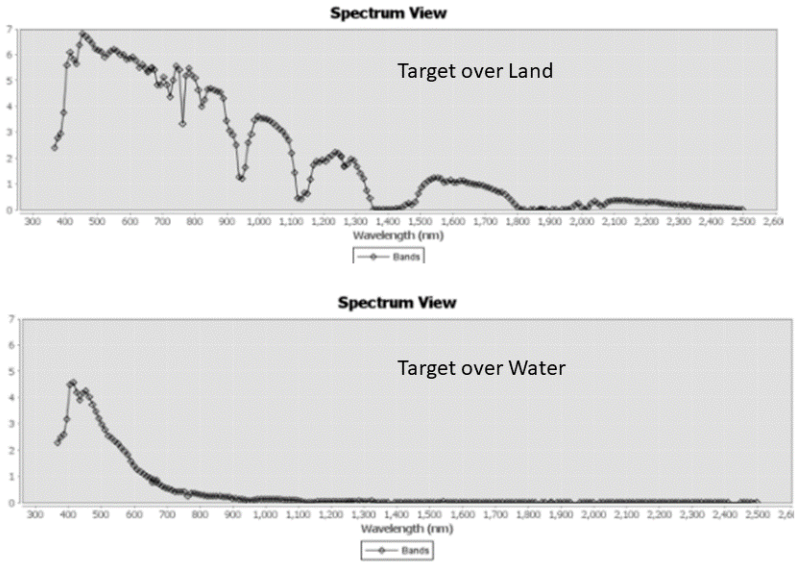

Figure 3.12: Example AVIRIS spectra over land and water

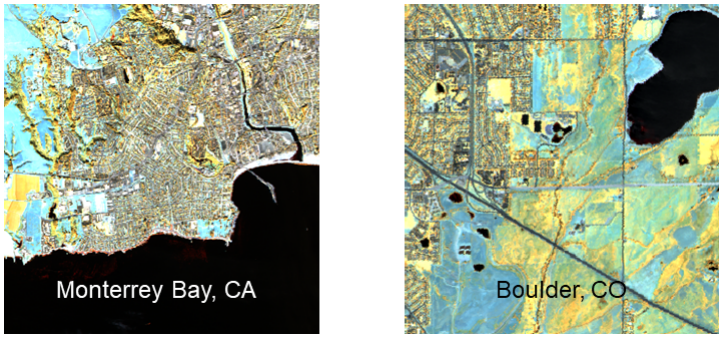

Figure 3.13: False color composites from AVIRIS acquisitions over Monterey Bay, CA and Boulder, CO

Chapter 4

GNSS as Signals of Opportunity

Global Navigation Satellite Systems (GNSS) consist of different constellations of satellites deployed by countries to provide global Position, Navigation, and Timing (PNT) services. Some of these constellations include the Global Positioning System (GPS) by the United States, GLONASS by the Russian Federation, Galileo by the European Union, and Beidou by China. There are also some Regional Navigation Satellite Systems (RNSS) that provide PNT services which include the NAVIC by India and QZSS by Japan. Receivers in the field of view of the satellite constellations measure the psuedoranges from different satellites after tracking the received signal and deriving the delay and doppler measurements. These measurements are the line of sight measurements where the only sources of perturbations include the satellite clock corrections, receiver clock corrections, tropospheric delay, ionospheric disturbances, the relative motion of the satellite with respect to the earth, and the geometry due to the rotation of the earth. These measurements had not been envisioned to be used for studying the earth's surface properties when the navigation systems were deployed [61].

GNSS Reflectometry (GNSS-R) is a new technology that is seeing constant development in oceanographic, land surface, and cryospheric applications [61]. The distortions in the code-correlator function after reflection or scattering of the GNSS signals from the earth's surface are used to sense the surface properties. This utilizes a type of system where the GNSS satellites form transmitters of a multistatic radar. GNSS signals lie in the microwave band of the electromagnetic spectrum, which generally covers the wavelengths between 1mm and 1m (300MHz and 300GHz). It

is one of those windows where the Earth's atmosphere is transparent and the signals can penetrate through the clouds. Thus, remote sensing of the earth's surface provides more observables as the signals can penetrate through atmospheric artifacts such as clouds [61].

4.1 Remote Sensing Methods

Remote sensing methods can be categorized into active and passive systems. Active microwave systems have evolved with the development of radar and use the relationships between the scattered cross-section with physical measurements such as ocean wind directions [42] and soil moisture [9]. The introduction of Synthetic Aperture Radar (SAR) has enabled the development of acquisitions with increased resolution. Radar altimetry can be used to measure land and ocean surface height measurements [19]. Passive microwave systems aim at measuring physical quantities from weak radiation emitted or reflected from the earth's surface across different wavelengths in the electromagnetic spectrum [86]. These radiations include natural emissions from different surface types. The measurements from these emissions are in the form of brightness temperature T_b, which is the equivalent temperature of a black-body radiator. The emissivity, ϵ, is a measure of the efficacy with which an actual surface at temperature T radiates as a black body ($T_b = \epsilon T$). The emissivity is empirically related to different physical measurements such as vegetation fraction [31], sea surface salinity [51], soil moisture content [41].

GNSS-R systems could be inferred as active systems, wherein they use artificially synthesized signals. They could also be characterized as passive systems as the receivers only need to listen to the reflected radiations from the earth's surface. Reflections from multiple transmitting satellites separated by hundreds of kilometers can be tracked simultaneously by satellite constellations placed in the Low Earth Orbit (LEO). Such systems require low power in comparison to monostatic radar configurations. Currently, there is growing interest among government and private agencies to deploy constellations of small satellites to explore different earth surface applications. These include the deployment of CYGNSS small satellites by NASA [73] and constellation by Spire Global [45] providing datasets for altimetry, tropical and cryospheric studies.

4.2 Initial Efforts in GNSS-R

There have been several efforts made in the development of deducing surface properties using reflected GNSS signals. Initially, GNSS-R was explored for oceanographic applications [40]. The Zavorotny and Voronovich model is based on Kirchhoff approximation to Geometric Optics. This is used in conjunction to either an ocean wave spectrum model [23] or an empirical slope distribution model [49]. This is to relate ocean surface winds to ocean surface roughness. GNSS-R was serendipitously developed during the calibration of the Shuttle Imaging Radar C-band. The reflections were captured from a probe at an altitude of 37km onboard a hot air balloon. These reflections were identified during the post-processing of the acquired data. A dedicated effort towards the development of the spaceborne GNSS-R was with the launch of the UK-DMC satellite. The measurements were recorded in the presence of collocated buoys to compare the satellite measurements to the in-situ measurements [34]. The GNSS-R measurements were used to calculate the ocean surface roughness [21]. The mission also collected a few batches of data over sea ice [32], and land surface [33] to develop an understanding of reflected signals from different kinds of surfaces. Following this, a dedicated spaceborne GNSS-R mission TechDemoSat-1 (TDS-1) [25] was launched in 2014 and the data was made public.

Under the NASA Earth Ventures program, the CYGNSS mission became a landmark development in spaceborne GNSS-R with the launch of a constellation of eight small satellites to study tropical regions. The small size and power requirements, along with the power to track simultaneous reflections with large separation has given rise to high temporal resolution. The low attenuation of signals at the L-band has also contributed to increased data coverage. This led to increased data collection to track hurricanes by monitoring the sea surface winds calculated using physical models on the GNSS-R observables. This helps observe rapid changes in tropical storms and depressions [72].

GNSS-R altimetry or Passive Reflectometry and Interferometry System (PARIS) [60] has been investigated with multiple airborne and fixed height experiments. Trends in the carrier phase

and signal strength measurements can be used for estimating inland and coastal water levels. Satellite-based GNSS-R altimetry has the potential to discern between ocean surface artifacts of different spatial scales in 10-100 km and repeat cycle of a few days. GNSS-R altimetry from orbit has its own set of challenges that include the low signal power and narrow bandwidth of open GNSS signals. For such reasons, steerable high-gain antennas and interferometric processing to make it possible with a scientifically useful error budget. These are backed by several fixed stations [69] and airborne experiments [29, 17].

Initial studies to estimate surface reflectivity by the means of reflected GNSS signals include the use of a signal antenna receiving the sum of direct and reflected signals [50]. Since these signals are superimposed, depending on the difference in path length, these signals would undergo constructive or destructive interference. The distance to the reflecting surface would also affect the frequency of power oscillations of the combined signal. The range of this variation is dependent on surface reflectivity. Such relations can be used to estimate sea level at an observed area [54], snow depth [55], soil moisture [87] and crop height [70]. These have been referred to as GNSS Multipath Reflectometry (GNSS-MR). Post such studies, there have been experiments that have used delay-doppler maps developed for oceanographic applications to extend towards soil moisture detection [87], sea ice condition and characterization mapping [71], inland water body detection, and river slope estimation [84]. Subsequent chapters will be discussing surface water detection using GNSS-R receivers.

4.3 Delay-Doppler Maps and Geometry

As mentioned earlier, passive microwave remote sensing provides observations that could be mapped to different geophysical variables such as ocean winds and sea surface height, along with the characterization of the scattering surface that could affect observable changes in an electromagnetic signal. Such mappings are referred to as Geophysical Model Functions (GMFs) [61], which include empirical elements from field experiments and several stages of calibration and validation of the remote sensing observables with respect to in situ measurements of the required geophys-

ical variables. These functions are valid for certain frequency ranges. GNSS-R observations are also passed through accepted functions to provide the required geophysical observations. These variables will depend on the perturbations of the GNSS signal reflections.

4.3.1 Delay-Doppler Mapping

Delay-Doppler Maps (DDMs) are essentially the fundamental observations provided by a GNSS receiver. It represents the distribution of the received signal power at a receiver with respect to a frequency offset f, and a time delay τ [61]. It can be defined as:

$$X(\tau, f, t) = \frac{1}{T_I} \int_{t-T_I}^{t} u(t)a(t-\tau)exp(-j2\pi ft)\, dt \tag{4.1}$$

This function is calculated by the cross-correlation of a local signal replica $a(t)$ with the received signal $u(t)$ for a coherent integration time T_I. This is similar to the DDMs used to signal acquisition and tracking, however, the received signal in this case is the reflected signal from a surface. Therefore, the distribution will be different as compared to tracking direct signals. Coherent integration times are limited to a few milliseconds, with a maximum cap of 20ms due to the low-rate data message at 50bps on L1 C/A. Time evolution of the scattering surface can cause signal correlation. To get sufficiently high SNR, the DDM samples undergo incoherent averaging of N_{inc} samples as:

$$Y(\tau, f) = \frac{1}{N_{inc}} \sum_{k=0}^{N_{inc}-1} |X(\tau, f, t_k)|^2 \tag{4.2}$$

Using GNSS-R DDM samples, essential information can be extracted for different geophysical variables that include sea surface height [16], ocean surface wind [48], ocean surface roughness [27], soil moisture [29], ocean tides [76] and terrain classification [36]. To assess these variables, it is imperative to know the types of geometry that the GNSS-R system uses, and the location of reflection points. These depend on the GNSS-R receiver location and the GNSS satellite transmitter.

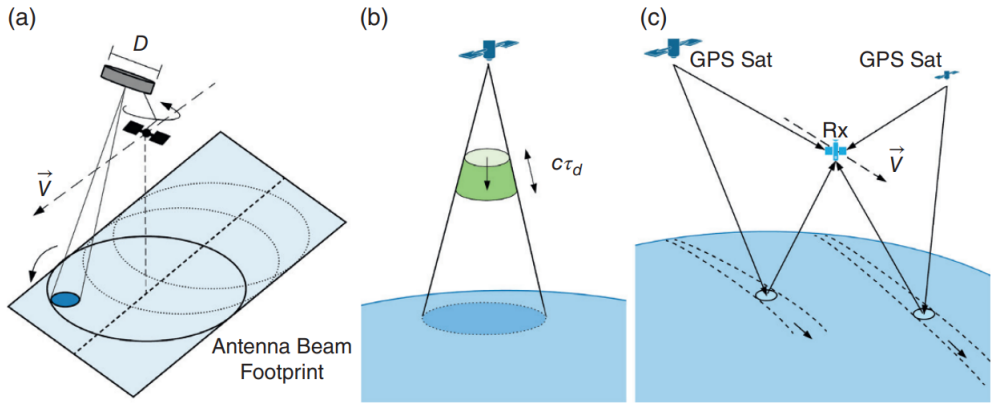

Figure 4.1: Different geometries of microwave remote sensing techniques. (a) represents passive radiometry; (b) shows a setup for active radar altimetry; (c) shows a schematic of the GNSS-R system. Source: [61]

4.3.2 GNSS-R Geometry

As mentioned earlier, microwave remote sensing could be categorized into two approaches - passive radiometry and active radar altimetry. In the case of a system based on passive radiometry, there is a single satellite whose antenna direction determines geolocation, whereas the antenna diameter determines the resolution. In the case of active radar altimetry, the pulse duration τ_d sets the resolution, while the antenna direction sets the geolocation of the measurement. In the case of GNSS-R, the resolution of the measurement is set by the transmitter bandwidth, while the geolocation is based on transmitter-receiver geometry [61]. This can be understood from Fig 4.1.

In the case of the GNSS-R system, the successful reception of a strong reflected signal will need the alignment of the transmitter and receiver antenna beams with respect to the incident and scattered ray paths respectively. The geolocation is however impervious to the steering of antenna beams as opposed to a monostatic radar [36]. The following section will deal with the determination of the locations on the earth's surface from where the GNSS signals are reflected and captured by a space-borne receiver.

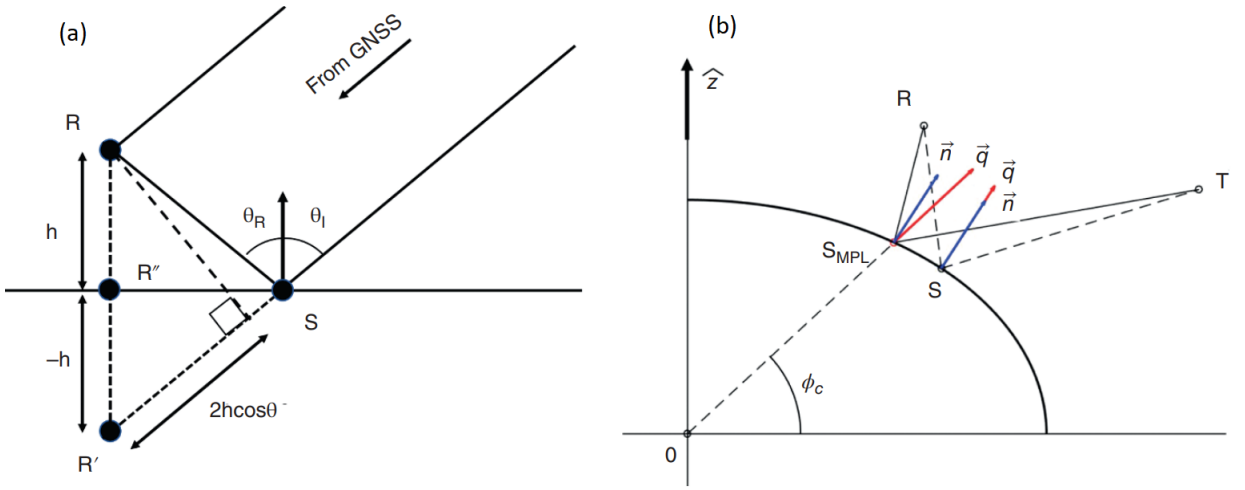

Figure 4.2: Geometries of GNSS-R systems with (a) airborne or fixed point receiver; (b) space-borne receiver. Source: [61]

4.4 Specular Points

The point on a reflecting surface and its surrounding region that contribute to the GNSS-R observation is called a specular point. It acts as a convenient origin point for a reference frame to compute the delay-doppler coordinates. In the case of an airborne or a fixed point GNSS-R receiver, a geometry as shown in Fig. 4.2(a) can be assumed, wherein the signals from the GNSS satellites can be assumed to be parallel. In that case, the reflecting surface can be assumed to be flat and level. If the receiver height is h from the surface, in that case, there will be an image of the receiver formed at a height $-h$ below the surface. In that case, given the receiver is the point R, the receiver image is $R^{'}$ and the sub-receiver point is $R^{''}$, the distance of the specular point from the point $R^{''}$ will be $r_s = h\ \tan\theta_I$. It will lie in the plane formed by T (transmitter), R, and $R^{''}$. Here, θ_I is the incident angle. However, for a space-borne receiver, the assumption of a flat and level reflecting surface will not hold. It will be under the purview of a geodetic survey, wherein the ellipsoidal nature of the earth's surface has to be taken into account. In such a case, an algorithm such as the Minimum Path Length (MPL) algorithm [61] has to be used.

4.4.1 Deriving the Specular Points

This sub-section describes the MPL algorithm to calculate the location of the specular points. As per Fermat's principle, an electromagnetic wave will be following the path with the shortest propagation time. As shown in Fig. 4.2(b), the vector from the origin of the coordinate system (origin of the ellipsoid) to the transmitter is $\vec{R}_T$, vector to the specular point is $\vec{R}_S$, and to the receiver is $\vec{R}_R$. The total path distance $\rho(\vec{R}_S)$ can be expressed as:

$$\rho(\vec{R}_S) = |\vec{R}_T - \vec{R}_S| + |\vec{R}_R - \vec{R}_S| \tag{4.3}$$

The specular point position $\vec{R}_S$ can be calculated by minimizing $\rho(\vec{R}_S)$ as per Fermat's principle, with the constraint that the point $\vec{R}_S$ lies on the surface of an ellipsoidal earth. Therefore, $\rho(\vec{R}_S)$ subject to the constraint:

$$g(\vec{S}) = \frac{1}{2}\vec{R_S}^T \mathbf{M}\vec{R_S} = 1 \tag{4.4}$$

where $\mathbf{M}$ characterizes the earth surface with a semimajor axis a and semiminor axis b a matrix of the form:

$$\mathbf{M} = \begin{bmatrix} \frac{2}{a^2} & 0 & 0 \\ 0 & \frac{2}{a^2} & 0 \\ 0 & 0 & \frac{2}{b^2} \end{bmatrix} \tag{4.5}$$

Now, the cost function for this constraint minimization problem is $J_{MPL}(\vec{R}_S) = \rho(\vec{R}_S)$, with the constraint in Equation 5.4. The corresponding gradient for the cost function would be:

$$\vec{\nabla} J_{MPL}(\vec{R}_S) = -\frac{\vec{R}_T - \vec{R}_S}{|\vec{R}_T - \vec{R}_S|} - \frac{\vec{R}_R - \vec{R}_S}{|\vec{R}_R - \vec{R}_S|} \tag{4.6}$$

Starting with an initial guess, $\vec{R}_S^{(0)}$, an iterative solution would be:

- Computer the gradient $\vec{\nabla} J_{MPL}(\vec{R}_S^{(n)})$.

- Change the estimate in the direction of steepest descent:

$$\vec{R}_S^{'} = \vec{R}_S^{(n)} - K\vec{\nabla} J_{MPL}(\vec{R}_S^{(n)}) \tag{4.7}$$

  K is the learning rate that could be set experimentally to attain acceptable convergence.

- Project $\vec{R}_S^{'}$ onto the ellipsoid:

$$\vec{R}_S^{(n+1)} = \frac{\vec{R}_S^{'}}{|\vec{R}_S^{'}|} r_e(\sin^{-1}(\frac{\vec{R}_S^{'} \cdot \hat{z}}{|\vec{R}_S^{'}|})) \tag{4.8}$$

  r_e depends on the geocentric latitude, ϕ_c as:

$$r_e(\phi_c) = \frac{ab}{\sqrt{a^2(cos)^2\phi_c + b^2(sin)^2\phi_c}} \tag{4.9}$$

The convergence is reached if, after several iterations, the position estimate change reaches below a threshold $|\vec{R}_S^{(n+1)} - \vec{R}_S^{(n)}| < \epsilon_{MPL}$. This method, however, leads to convergence with bias. This bias can be reduced by projecting the gradient to the constraint surface:

$$\vec{R}_S^{'} = \vec{R}_S^{(n)} - K(\vec{n}(\vec{R}_S^{(n)}) \times \vec{\nabla} J_{MPL}(\vec{R}_S^{(n)}))) \times \vec{n}(\vec{R}_S^{(n)}) \tag{4.10}$$

where the direction normal to the ellipsoid is given by:

$$\vec{n}(\vec{R}_S) = \mathbf{M}\vec{R}_S \tag{4.11}$$

4.4.2 Fresnel Zones

After the calculation of the specular points, it is important to understand the fresnel zones of the reflections. The carrier phase remains close to the minimum value in the vicinity of the specular point, while it is stationary at the specular point. The points within half-wavelength, $\lambda/2$ of the specular point is the First Fresnel Zone (FFZ) [43]. Outside this region, there will be constructive and destructive interference that is spread till the final scattered field, canceling out their contributions [10]. In case there is partial illumination of the Fresnel zones due to reasons such as the presence of an obstruction, the surface integral becomes truncated, giving rise to diffraction effects [28].

4.5 Surface Properties from Reflected Signal

The carrier phase measurements depend on the total path delay after the reflection, along with the undulations in the surface. From a smooth surface, the reflections tend to be very concentrated in a particular direction, rendering it to be specular. However, as the surface becomes rougher, the glistening zone increases, due to which the reflections can be spread out in different directions, which will be diffused. This also has an effect on the nature of carrier phase measurements that is useful in characterizing the observed surface.

4.5.1 Cross-correlation waveforms

DDM forms the fundamental observation from a GNSS receiver, formed by the cross-correlation of the received reflected signal with a local replica across different doppler shifts and delay bins. The shape of a DDM can be used to characterize the roughness of the reflecting surface. For a perfectly flat surface, the ray of GNSS signal will be reflected towards the receiver, thus the signal structure will be similar to that of a direct signal, with an additional delay of τ_s and power attenuation proportional to the extra distance traveled [61]. The DDM will look equivalent to the Woodward Ambiguity Function (WAF) of the transmitted GNSS signal shifted by τ_s. When the surface becomes rougher, the slopes can be considered as small mirrors that can reflect the rays of GNSS signals in a direction away from the receiver [61]. This will make the reflections diffused, and the peak power would decrease at the specular path delay τ_s and more power will show up in the tail of the DDM. This is seen in Fig. 4.3. The more the roughness of the surface, the more there is a reduction in the power of the reflected signal.

As observed, the amplitude of the DDM is representative of the surface properties. In the case of a perfectly smooth surface, the reflected signal amplitude could be given by the Fresnel reflection coefficients, describing the energy reflected into the specular direction v/s observed by the scattering medium. In the case of a non-magnetic surface, the copolar reflection coefficients can be given by:

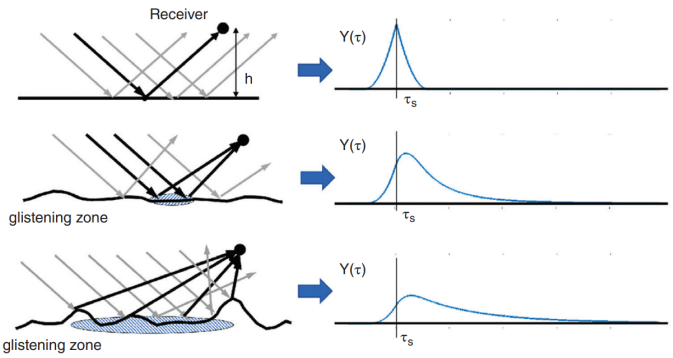

Figure 4.3: DDM at a doppler shift for (a) very smooth surface; (b) a bit of rough surface; (c) a very rough surface. As the surface becomes rougher, the glistening zones enlarge and the received power reduces. Source: [61]

$$R_{HH} = \frac{\cos\theta - \sqrt{\epsilon_r - \sin^2\theta}}{\cos\theta + \sqrt{\epsilon_r - \sin^2\theta}} \tag{4.12}$$

$$R_{VV} = \frac{\epsilon_r\cos\theta - \sqrt{\epsilon_r - \sin^2\theta}}{\epsilon_r\cos\theta + \sqrt{\epsilon_r - \sin^2\theta}} \tag{4.13}$$

Here, R_{pq} is the Fresnel reflection coefficient where p indicates the incident polarization and q indicates scattered polarization. The local incident angle is given by θ and ϵ_r is the complex dielectric constant of the surface. A GNSS signal is transmitted as a Right-Hand Circularly Polarized (RHCP) signal, which after reflection also has a Left-Hand Circularly Polarized (LHCP) component. The circularly polarized components can be a linear sum of R_{HH} and R_{TT}, as given by:

$$\begin{bmatrix} R_{LL} & R_{LR} \\ R_{RL} & R_{RR} \end{bmatrix} = \frac{1}{2}\begin{bmatrix} R_{HH} + R_{VV} & R_{HH} - R_{VV} \\ R_{HH} - RVV & R_{HH} + R_{VV} \end{bmatrix} \tag{4.14}$$

For a flat surface, the reflectivity can be calculated by using the Fresnel reflection coefficients:

$$\Gamma_{pq} = |R_{pq}|^2 \tag{4.15}$$

4.5.2 Phase Observations

Reflected signal path introduces an additional path delay as the waves have to travel a longer distance. The phase difference between the direct and reflected signals can be measured by complex cross-correlation of waveforms that provide precise ranging observables [61]. Such observations are useful in applications such as seasonal sea ice variation. The phase measurements can be acquired only over calm surfaces, limiting their application to inland water bodies. Such phase measurements tend to be similar when acquired by space-borne receivers and have fewer differences amongst each other since the surface geometry tends to be homogeneous as compared to the wavelength of the signals [61]. The path differences are not large across consecutive samples over reflections over water, which render the reflections to be coherent. Coherency detection over inland water bodies using phase measurements is further elaborated upon in Appendix B.

Chapter 5

Surface Water Detection using GNSS-R

Freshwater is a necessity for the sustenance of human population centers and their anthropogenic activities. Therefore, it can be found that most of these centers are located near inland water bodies. Thus, to better manage freshwater sources, it is important to map out their extent and use them for effective policy making. Water supply distribution to urban and rural regions, storm management, and disaster mitigation comprise of some of the important aspects that need consistent monitoring and processing of remote sensing data. GNSS-R data have been used for applications over inland water bodies due to their demonstrated higher sensitivity to surfaces that are relatively calmer than oceans. It has been demonstrated by [88] that GNSS reflections over water bodies can be isolated using Signal-to-Noise Ratio (SNR) and carrier phase measurements. In this chapter, detecting inland water bodies using SNR and optical remote sensing data measurements is studied, corroborated by coherency in carrier phase measurements.

As mentioned in the previous chapter, GNSS-R is of rising interest among public stakeholders. Spire Global has developed and deployed a constellation of GNSS-R receiver satellites in the Low Earth Orbit (LEO) to acquire bistatic radar measurements at a low grazing angle [46]. The data products have been used for studies on sea surface altimetry, sea ice, and inland water bodies. CYGNSS [63], TechDemoSat [57] and Spire Global [88] data products have been used in the past to study inland water bodies mostly in the tropical region and wide rivers such as the Amazon river [47].

Essentially, isolation of specular reflections over inland water bodies is a classification problem

that has been approached using Kalman filters [44], sensitivity to SNR [88], and using multi-sensor data [75]. An experiment using Kalman filters as demonstrated by [44] was done with airborne measurements. To carry out similar studies with space-borne receivers, the footprint of reflections must be similar, which is not the case. Using sensitivity to SNR and coherency in reflections has been demonstrated to show accurate classification [88], but these studies have been done over wide rivers or lakes, which have many contiguous specular reflections over water. This is not always the case as river systems can become winding, so a single track can have reflections straddling over water and land. Using multi-sensor data has shown promising results in achieving accurate classification of specular reflections [75] with Sentinel-1 backscatter coefficients, Normalized Difference Vegetation Index (NDVI) measurements from Sentinel-2, and measurements from airborne GNSS receivers.

GNSS-R systems have the potential to cover large areas of the earth's surface with a high repeat cycle. Due to the increased availability of datasets, it provides an option to monitor inland water body dynamics along with legacy sensors to provide hydrologists with automatically segregated specular reflection measurements to perform altimetry. These datasets can be used to measure water body extent and river flow. Carrier phase measurements have been used [22][71][85] for coherency detection to identify water bodies. This has not been used in this study for an application in developing an onboard GNSS-R data collection system to automatically retain I/Q measurements which can be used to derive the phase measurements. With these applications in consideration, this and the subsequent chapter will deal with the study on the following objectives:

- Segregate specular points over inland water bodies and land over a study area.
- Accuracy assessment of the classification based on Spire GNSS-R data.
- Generate a map of the specular points over water for a month to show the water body extent.
- Generate windows of reflections over water bodies that have more than 5 samples of measurements over water.

Figure 5.1: Study area with the gauge stations in the area in the US [62]

5.1 Study Area and Dataset

Datasets acquired by Spire Global over the Lower Mississippi River Basin have been studied. The tracks of the Spire Global grazing angle dataset were selected and the inland specular points were selected using the North American political boundary provided by USGS [2]. The study area is shown in Fig. 5.1.

The grazing angle dataset by Spire Global [46] is acquired by GNSS bistatic radar measurements from reflections at a low grazing angle. As mentioned, these datasets have been used in several cryospheric, land, and oceanographic applications. The satellites are equipped with GNSS receivers that collect reflected signals with limb facing Right Hand Circularly Polarized (RHCP) antennae directed towards the limb of the earth. The geometry for GNSS-R acquisitions by Spire is shown in Fig. 5.2. Over smooth surfaces, the measurements are expected to be coherent. The Spire Global satellites acquire measurements on L1 and L2 bands. In this study, the SNR measurements in volts/volt (v/v) on the L2 band are used to isolate reflections over water due to their higher sensitivity to water[88].

In addition to the GNSS-R measurements by Spire Global, the Normalized Difference Vegetation Index (NDVI) was calculated from the optical reflected radiance data collections from the

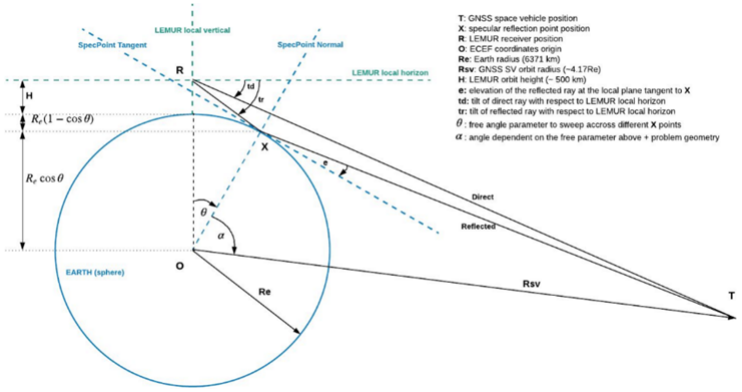

Figure 5.2: Spire LEMUR GNSS receiver geometry [46]

Sentinel-2 mission along with backscatter coefficients from Sentinel-1 Synthetic Aperture Radar (SAR). The Sentinel-2 acquisitions are available every 6 days at 20m spatial resolution due to two satellites in its constellation, Sentinel-2A, and Sentinel-2B. The NDVI is calculated using red and near infra-red surface reflectances as per [75]. Sentinel-1 acquisitions are available for two transmitter-receiver polarization configurations every 5 days: Vertical-Vertical (VV) and Vertical-Horizontal (VH). In this study, for a given track, the Sentinel-1 and Sentinel-2 acquisitions are taken in a window of ± 5 days of the track acquisition date in June 2021. These measurements are used along with the L2 acquisitions from Spire due to the possibility of measurements from specular points straddling water and land with similar SNR values. Such additional features are needed to obtain a distinct characterization of specular points.

The Global Surface Water Explorer (GSWE) provides occurrence and seasonality data derived from the Landsat mission from the year 1984 till 2021 for inland water bodies[66]. As apriori data, the occurrence values from the GSWE are used to compare the classification results using Spire and Sentinel measurements for accuracy assessment.

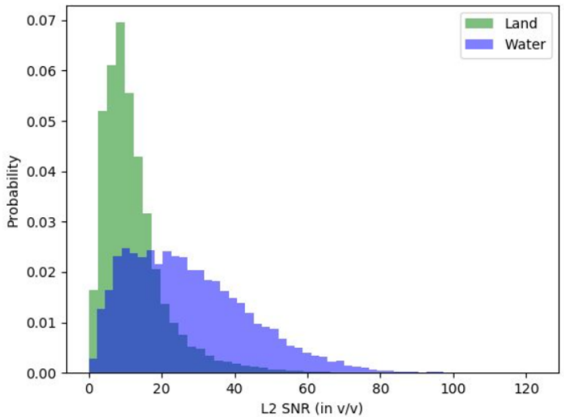

Figure 5.3: Probability distribution of L2 SNR over land and water.

5.2 Methodology

5.2.1 Data pre-processing

Using the USGS North America political boundary [2], the Spire measurements over the Lower Mississippi River basin in Louisiana and Mississippi states were retained. The acquisitions from Sentinel-1 and Sentinel-2 were extracted using the Google Earth Engine [35] from the Copernicus datasets [1] as mentioned earlier. Google Earth Engine is also used to extract the GSWE data for water occurrence. Histogram in Fig. 5.3 shows that reflections over water and land can have strong overlaps in SNR levels. However, there are higher chances that reflections over water will have higher SNR. Therefore, the relationship between the GNSS-R measurements and optical indices from Sentinel-2 is studied by comparing classification based on GNSS-R measurements, NDVI, and both. This is further elucidated in the upcoming sections.

5.2.2 Classification Algorithm

In this study, based on the different assignments on the SNR, NDVI, and backscatter measurements, the classification of specular points is done. As seen from Fig. 5.3, the SNR of reflections over water tends to be on the higher side. Therefore, different thresholds on SNR and their classification accuracy have been studied. Along with the threshold set on the SNR, limits were also set on

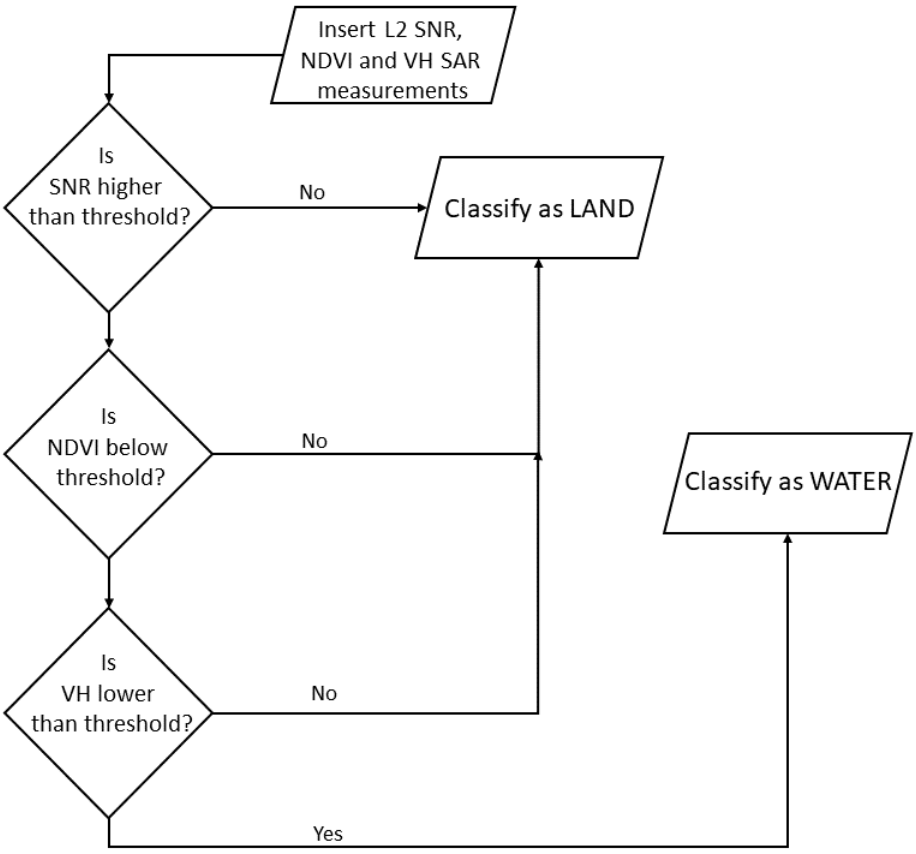

Figure 5.4: Threshold-based classification algorithm

the NDVI values. Since reflections in the NIR band are less in proportion to those in the red band, the NDVI values for reflections over inland water will be negative, or near zero. Therefore, different NDVI thresholds have also been studied since points over water can also have positive NDVI due to higher turbidity. A single threshold has been set on the SAR measurements to account for NDVI acquisitions under cloudy scenarios. A schematic of the classification algorithm is shown in Fig. 5.4. In the upcoming sections, trends of SNR values with NDVI (used along with SAR backscatter) will be discussed.

5.2.3 Metrics for Classification Accuracy

Three different metrics are used to assess the quality of the binary classification mentioned in Section 5.2.2. These are namely True Positive Rate (TPR), False Positive Rate (FPR) and False Discovery Rate (FDR). These are defined as:

$$TPR = \frac{TP}{TP + FN} \tag{5.1}$$

$$FPR = \frac{FP}{FP + TN} \tag{5.2}$$

In Equations 5.1, 5.2, True Positive (TP) denotes the number of samples that have been correctly classified as positive, False Positive (FP) denotes ground truth negative samples incorrectly classified as a positive. True Negative (TN) denotes the number of correctly classified as negative, and False Negative (FN) denotes the number of ground truth positive samples incorrectly classified as negative. Therefore, TPR determines the proportion of correct positive classifications among ground truth positives, FPR tells the proportion of false positive classifications amongst the ground truth negatives. This can also be realized with the help of an example confusion matrix in Fig. 5.5. For the context of this study, reflections over water are categorized as positives, and those over land as negatives.

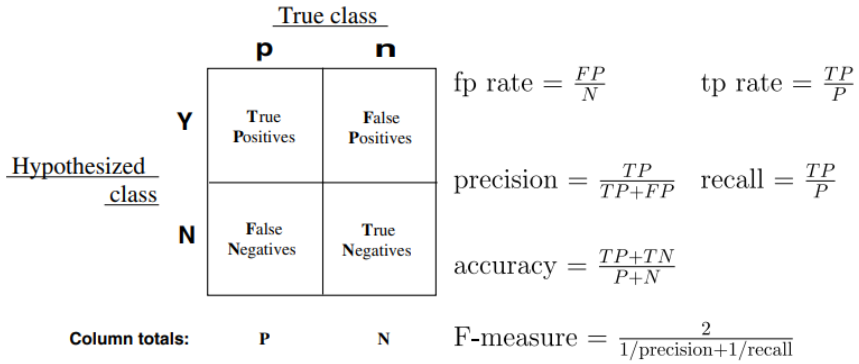

Figure 5.5: Example confusion matrix showing True Positives (TP), False Positives (FP), True Negatives (TN) and False Negatives (FN) used to define metrics to assess classification quality [24].

5.3 Observations

Before assessing the classification accuracy based on different thresholds, it is important to discuss the trends that lead to attempt classification using the SNR of L2 reflected signals, NDVI, and SAR backscatter measurements. As seen from Fig. 5.6, we can see that data points over the Mississippi river have lower values of NDVI and SAR measurements.

As seen from Fig. 5.7, data points over water tend to have negative or near zero NDVI values. The points also tend to have higher L2 SNR measurements, which is also shown in Fig. 5.3. Due to a distinct difference in the values of measurements forming separate classes, a threshold can be put on the L2 SNR and NDVI measurements to implement a classification algorithm mentioned in Section 5.2.2.

A threshold is also put on the backscatter measurements. This is because NDVI measurements can be erroneous due to the presence of clouds. In such a case, points over land bodies can have negative NDVI values, as seen in some of the data points in Fig. 5.7. To avoid them, the backscatter coefficients are also used to identify smooth surfaces that have high forward scattering. As seen from Fig. 5.8, the backscatter coefficients have lower measurement values over water when compared to land. This is because since inland water bodies have smoother surfaces as compared to the surrounding land, the backscatter is less. It is similar to the explanation for higher SNR

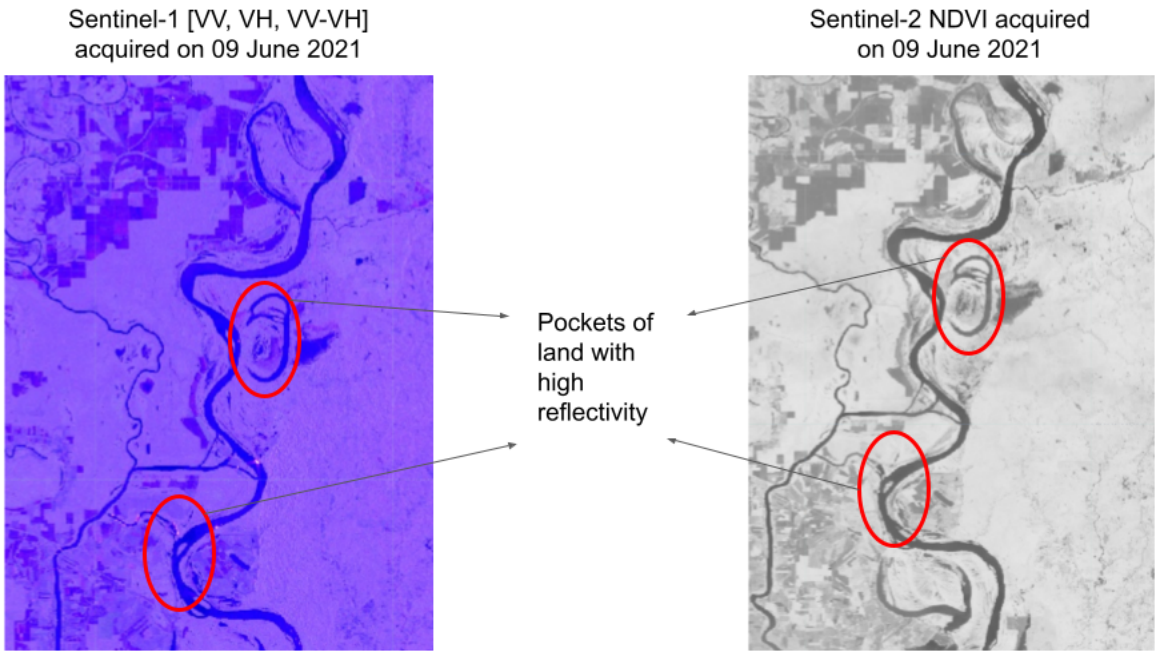

Figure 5.6: Distinction in measurement of backscatter coefficients from Sentinel-1 and NDVI from Sentinel-2. Darker shades represent lower values of measurements.

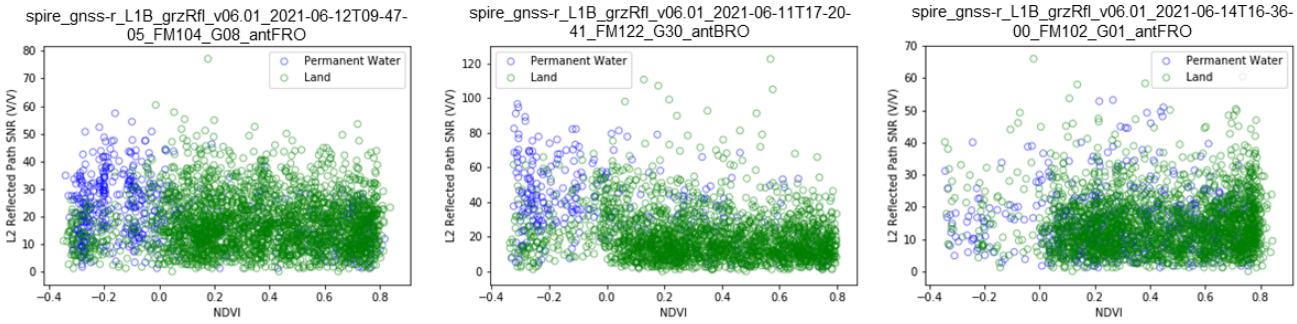

Figure 5.7: L2 SNR v/s NDVI for three Spire tracks over land and water.

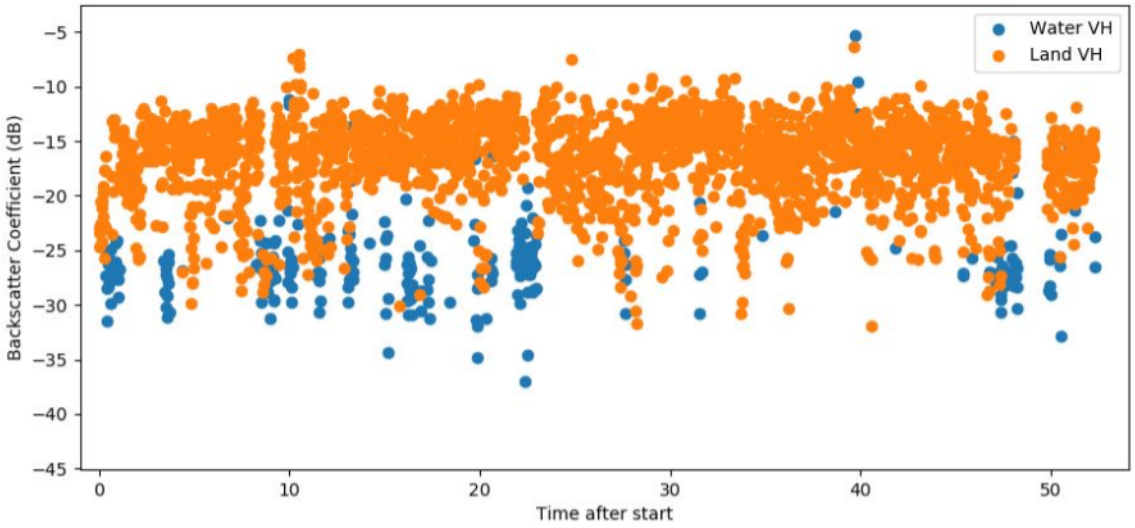

Figure 5.8: SAR backscatter coefficient measurements along a Spire track over points on water and land.

values for L2 GNSS measurements. These observations form the basis of using the NDVI, SAR, and GNSS-R measurements for this classification. In the next section, the classification accuracy due to different thresholds is assessed.

As mentioned in Section 5.1, L2 SNR values are more sensitive to reflections from water as compared to L1 SNR. This can also be seen by plotting L2 SNR v/s NDVI and L1 SNR v/s NDVI, where it could be seen that reflections over water are not able to form a distinct cluster when L1 SNR and NDVI are used for classification, while L2 SNR is able to do so along a Spire track as shown in Fig. 5.9. It is because more number of reflections from water are having a higher SNR value in L2 band than in L1 band. It can be seen that for the Spire track shown in Fig. 5.9, the L1 SNR values over water are mostly concentrated between 10-60v/v, while for L2 SNR, the cluster of measurements is spread between 10-80v/v.

5.4 Results

In this section, classification with the help of NDVI and VH SAR measurements only, with the help of L2 SNR only, and classification algorithm mentioned in Section 5.2.2 are assessed. In the available dataset, there were 356,338 points, among which 341,291 were over land (with occurrence

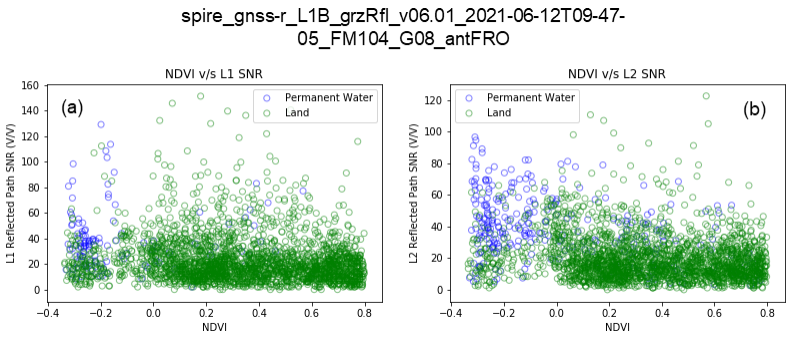

Figure 5.9: Comparing L1 and L2 SNR v/s NDVI to demonstrate the sensitivity of L2 SNR towards reflections from water as compared to L1 SNR.

value less than 80% on the GSWE data), and 15,047 over water bodies or with occurrence value over 80%. This dataset is therefore unbalanced. Classification quality is assessed on a balanced dataset where the number of samples over land is equated to those over water by randomly selecting samples among ground truth land. The metrics in Equations 5.1 and 5.2 are calculated by randomly selecting samples over ground truth negatives 20 times and their mean is taken to form Mean TPR and Mean FPR.

The performance of classification using different L2 SNR thresholds is assessed, without involving NDVI. In this case, the L2 SNR threshold is varied from 10v/v to 50v/v at an interval of 2v/v. The samples having L2 SNR above these thresholds are classified as positives. The TPR and FPR across different L2 SNR thresholds are observed. The FPR shows a decreasing trend from about 50% for a threshold of 10v/v, to less than about 10% for a threshold of 50v/v for the balanced dataset. A similar trend is observed for TPR, with value of about 85% for an L2 SNR threshold of 10v/v, monotonically decreasing to values around 10% as the L2 SNR threshold increases. This is also seen in Fig. 5.10. It shows that the proportion of true classification of samples as a reflection over water among the ground truth negatives decreases as the L2 SNR threshold increases. The FPR shows a decreasing trend with increasing SNR, because lesser number of points among ground truth reflections over land will be classified as positives. This is due to the fact that reflections over inland water will be having higher SNR than those over land [61]. Increasing the threshold will thus reduce the number of positives by limiting the number of reflections having SNR higher

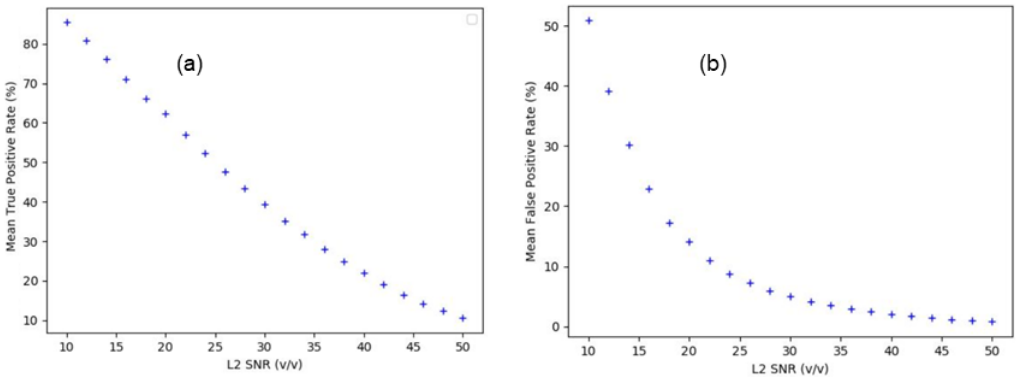

Figure 5.10: (a) Mean True Positive Rate (TPR) and (b) Mean False Positive Rate (FPR) for varying L2 SNR thresholds, calculated over balanced dataset. In this case, all the samples that have an L2 SNR measurement more than the threshold values are classified as positive.

than the threshold.

In order to determine a good threshold of NDVI for classification, the variation of TPR and FPR is studied across three NDVI values; 0, 0.05 and 0.1. As it is observed, higher NDVI threshold can lead to higher FPR and TPR when classification is done only using NDVI and VH measurement. This is also seen in Fig. 5.11. As seen, the proportion of the true positive classifications among the ground truth positives is approximately 73% when the NDVI threshold is 0. It further increases as the threshold increases to a certain limit due to the inclusion of more samples that can be classified as positive, but the rate of increase in TPR decreases as there are less number of samples that have an NDVI value between 0 and 0.1 over water than the number of samples with NDVI less than 0.

The TPR and FPR are also calculated across different L2 SNR and NDVI thresholds to investigate the quality of classification when both L2 SNR and NDVI thresholds are used. In this case, the samples that have L2 SNR values more than the threshold, and NDVI measurement less than the threshold are classified as positive. The TPR and FPR values see a significant change in comparison to classifications that use only NDVI or L2 SNR measurements. This is shown in Fig. 5.12. As seen for classification with using only L2 SNR for, TPR and FPR decrease monotonically with increasing L2 SNR threshold.

Fig. 5.13 shows the Receiver Operating Characteristic Curve (ROCC) formed by plotting

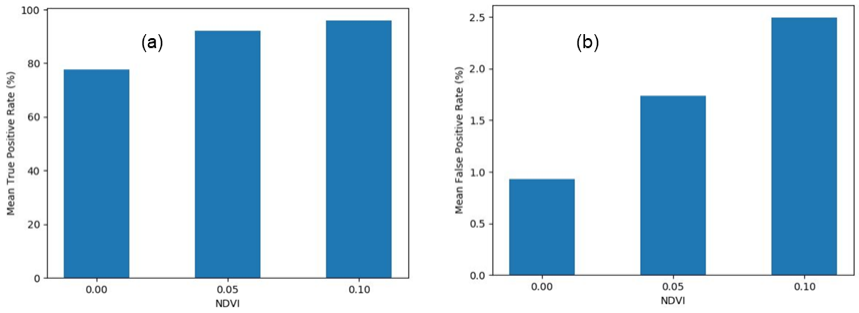

Figure 5.11: (a) Mean TPR and (b) Mean FPR for varying NDVI thresholds, calculated over balanced dataset. In this case, all the samples that have an NDVI value less than the threshold values are classified as positive.

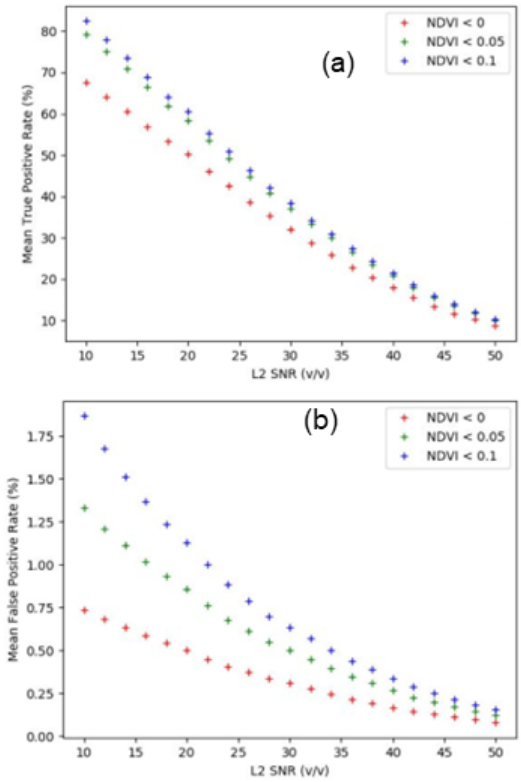

Figure 5.12: (a) Mean TPR and (b) Mean FPR v/s L2 SNR thresholds for varying L2 SNR and NDVI thresholds, calculated over balanced dataset.

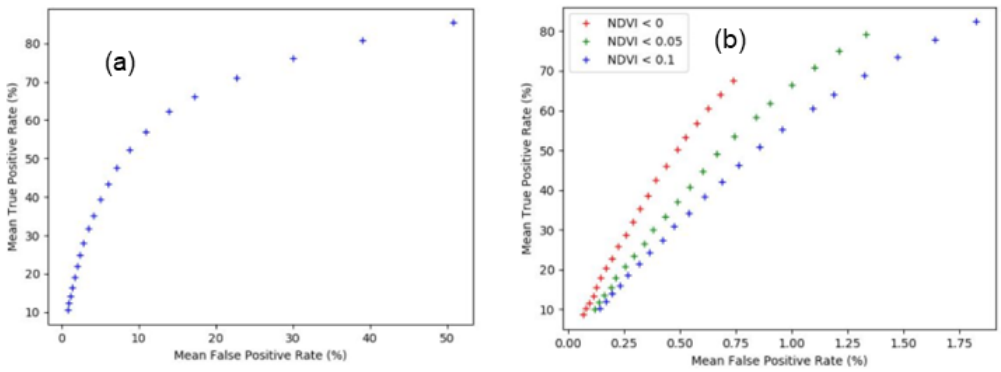

Figure 5.13: ROCC of classification using (a) only varying L2 SNR threshold with an interval of 2v/v; and (b) varying both L2 SNR (at an interval of 2v/v) and NDVI thresholds (0, 0.05 and 0.1).

the TPR v/s FPR for classification using both L2 SNR and NDVI thresholding, and classification using only L2 SNR thresholds. In both cases, when the FPR is reduced, the TPR also reduces, thereby deteriorating the classification quality.

In a Receiver Operating Characteristic (ROC) space, an ideal classifier can be determined by an algorithm providing a TPR of 100% and FPR of 0%. A conservative classifier would have a TPR of 0% for an FPR of 0%, which means more evidence would be required to correctly classify a sample as positive. A liberal classifier would be having a TPR of 100% for an FPR of 100%, meaning a sample could be easily classified as positive which would be highly likely to be incorrect [24]. As seen in Fig. 5.13(a), as the TPR and FPR increase, the classification becomes more liberal, meaning there is a higher possibility of inaccuracy in detecting reflections over water. There would be a higher chance to falsely classify a reflection over land as one over water. However, as seen in Fig. 5.13(b), the TPR increases with only a slight increase in FPR. While the general trend is towards the classification being more liberal, L2 SNR and NDVI thresholds make the classification more accurate (closer to an ideal classifier). This is in a manner showing that L2 SNR and NDVI complement each other to make better classification of reflections over land and water. This can be explained by the fact that the L2 SNR is able to identify the points that are covered by clouds but can be potentially over land. In such a case, the L2 SNR will have a smaller value than over water, while the NDVI will be negative due to cloud presence. This will make the classification

to be one over land. On the other hand, NDVI is able to identify points over land that can have high SNR due to it being smooth or temporarily inundated with turbid water. In such a case, the NDVI can be positive, and the SNR will be high. Therefore, it would be classified as a negative, or a reflection from land. From the ROCC in Fig. 5.13(a), plots in Fig. 5.12 and Fig. 5.11, taking the NDVI threshold as 0 and an L2 SNR threshold between 15-20v/v can have a TPR between 55-70%. In cases NDVI is contaminated due to cloud cover, taking the same L2 SNR threshold would have a slight change in TPR, but significant change in FPR, meaning there would be higher number of samples classified as a reflection over water even though it could be one over land.

The experiment of classification using thresholds is undertaken for several tracks. These cover a significant area of the Lower Mississippi Basin. Over June 2021, all the specular points isolated over water are aggregated to produce a map as shown in Fig. 5.14. As seen over some points on a track in Fig. 5.15, the reflections are straddling over water and land. Therefore, the coherency detector in [71] is providing erroneous classifications, since a window is having points over both land and water. Due to this, the circular length value dips leading to reflections over water classified as semi-coherent or incoherent in some cases. Therefore, the aggregated points in Fig. 5.14 provide with means to create windows that exclusively have reflections over water, which may be discretely distributed.

Fig. 5.16(a) shows the distribution of window lengths from the ones derived after aggregating the classified points (with L2 SNR threshold of 16v/v and NDVI threshold of 0) from all the tracks in June 2021. It is seen that 50% of the reflections are isolated, while more than 85% of the reflections have less than 5 samples in a window. Windows of more than 5 samples and a maximum of 15 samples have been made and the coherency detector defined in [71] is used to calculate the circular length that works as a coherency detector. As seen in Fig. 5.16(b), more than 50% of the windows have a circular length of 0.97, while the average is 0.94. This leads to the derived windows having highly coherent reflections. Fig. 5.16(c) shows the color-coded circular length calculated as defined in [71] using the phase-noise method. The circular lengths are calculated using the carrier phase measurements of the specular points identified as water using L2 SNR threshold of 16v/v

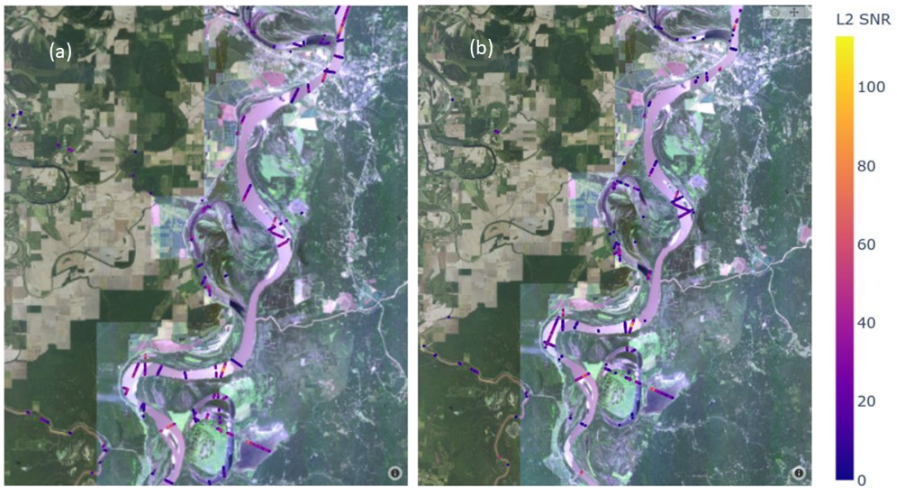

Figure 5.14: (a) shows the map with the ground truths over water; (b) shows the points over water when the L2 SNR threshold as 16v/v and the NDVI threshold is 0. The color bars show the L2 SNR in v/v over the specular points. It is oberved that there are several points in (b) that have been classified as water, which as per (a) do not form a part of the set of ground truth positive samples. Thus, these points are classified as false positives.

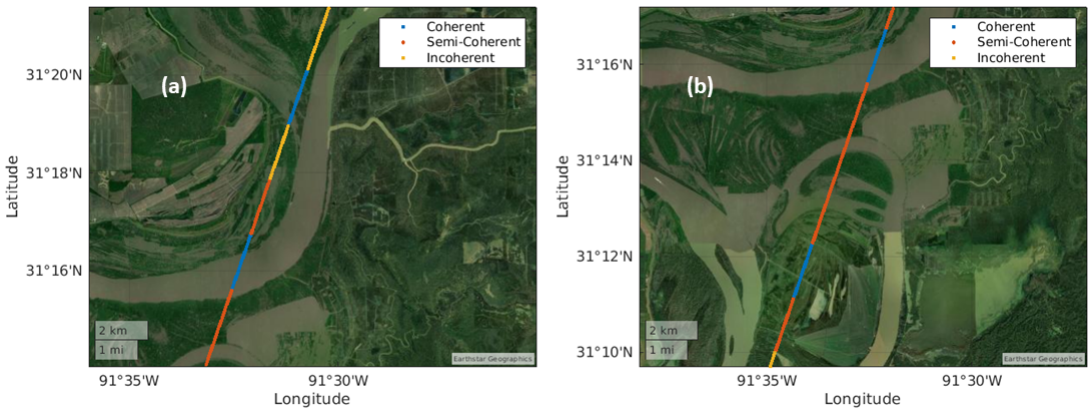

Figure 5.15: Instances of the river snaking along a track, where coherent reflections are observed over water as seen in (a), while there are some semi-coherent reflections over water as seen in (b) where the windows of detection do not have a sufficient amount of reflections over water.

and NDVI threshold of 0.

5.5 Discussions

The study described in this chapter and the observations demonstrate a potential application of GNSS-R in addition to optical and radar imagers for specular point classification over land and water. Data from multiple sensors help in mitigating the consequences due to the larger footprint of reflection for space-borne GNSS-R receivers. The high repeat cycle of GNSS-R acquisitions makes it possible to cover a large area with high temporal resolution. This is necessary to study surface water dynamics daily. The classified specular points from multiple tracks can be aggregated to form a map as the one shown in Fig. 5.15. As mentioned in the previous section, a point can be classified with a true positive rate of 55-70% depending on the different L2 SNR thresholds in 15-20v/v and the NDVI threshold as 0. Classification with only L2 SNR will lead to higher chances of negative samples being classified as a positive. NDVI and L2 SNR would also complement each other to make more accurate classifications. An L2 SNR threshold lower than 15v/v might seem to be able to provide more accurate classification in terms of TPR and FPR, but the signals as per the measured SNR would be closer to the noise floor determined by [88]. Keeping a lower L2 SNR threshold will retain several specular points that can be potentially classified as over water as the distribution of L2 SNR over land and water overlap significantly. Therefore, an L2 SNR threshold of approximately 16v/v along with NDVI threshold of 0 will be able to retain a significant number of specular points over water with a low rate of misclassification of points that are actually over land. Fig. 5.17 shows heatmaps generated after classification only using NDVI, only using L2 SNR threshold of 16v/v, and using both L2 SNR and NDVI thresholds to show the distribution of samples into different categories post classification to calculate accuracy metrics. Since intermittent reflections are straddling between land and water, GNSS-R measurements alone cannot be used, and coherency analysis would require an algorithm that would be able to isolate windows that have reflections over water only. The land around the river can also be inundated or smooth as compared to the wavelength of the GNSS signals which can lead to high SNR and coherent reflections due to

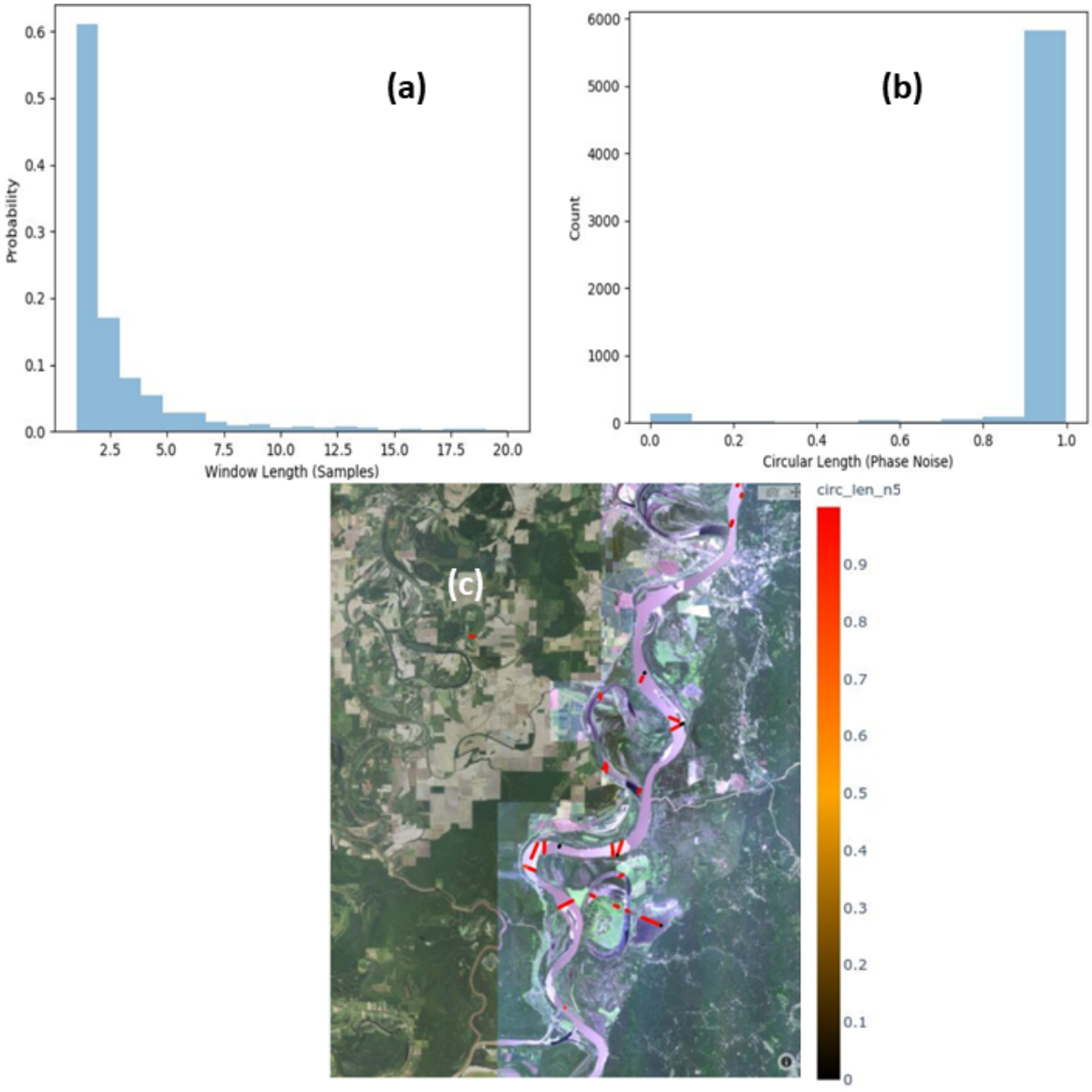

Figure 5.16: (a) Probability distribution of window lengths of contiguous reflections over surface water after segregating with the algorithm stated in Section 5.2.2; (b) Histogram of the circular length of the phase measurements from the points in windows having more than 5 reflections over water; (c) Specular points detected over water, with color-coded circular length when coherency is detected using phase noise. The specular points have been classified with L2 SNR threshold is 16v/v and NDVI threshold of 0.

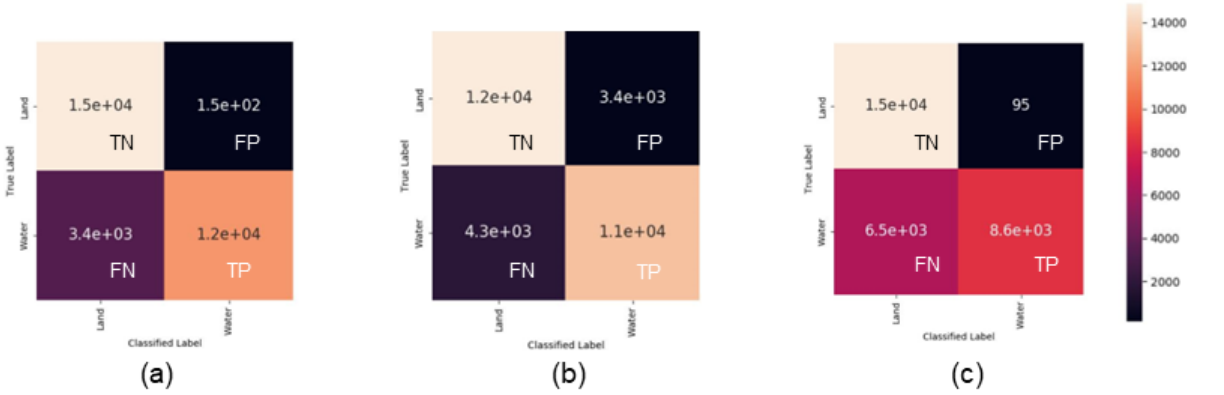

Figure 5.17: Heatmaps after classification showing the number of classified samples as TP, TN, FP and FN on balanced dataset. (a) is the heatmap generated after classification only using an NDVI threshold of 0 and VH measurement threshold of -22dB; (b) shows the heatmap after only L2 SNR threshold of 16 v/v and no use of NDVI in classification; and (c) shows the heatmaps after classification using L2 SNR threshold of 16 v/v, NDVI threshold of 0, and VH measurement threshold of -22dB.

the presence of agricultural fields. These can lead to missed and false detections. Therefore, such studies are required to develop algorithms to automatically segregate reflections over water and develop datasets for altimetry applications over rivers to develop sustainable hydrological resource management policies directed to fulfill the U. N. Sustainable Development Goals (SDGs)

Chapter 6

Conclusion

In this thesis, surface water detection using optical and reflected GNSS signal measurements is discussed. It is studied that due to high spatial resolution, it is possible to discern between inland water bodies due to their difference in reflected radiance in the NIR region. Towards the development of such instruments with lesser complexity, a spectral super-resolution algorithm is studied that implements dictionary learning followed by random forest regression. It is observed that over the training area, the quality of signal reconstruction is measured with an IRD of 31.58dB. The same algorithm is also implemented for acquisition tracks over different study areas, with reconstruction happening at a maximum IRD of about 20dB.

It is also observed that there are optical payloads that provide data at a high spatial resolution, the repeat period to cover a track is large. This means the measurements are not available with a high temporal resolution making it difficult to study inland water bodies. Due to this, reflected GNSS signal measurements are studied along with optical and SAR backscatter to identify inland water bodies. It is seen that carrier phase measurements have been used previously to do this, but mostly in applications of lakes and wide river bodies. However, when it comes to narrow rivers, water body detection using carrier phase measurement does not function properly as a window selected has intermittent reflections straddling between land and water, thereby not providing proper coherency statistics for detection. Introduction of optical data to reflected GNSS signal SNR can perform a threshold-based classification which, in this thesis, shows around 55-70% TPR to classify a reflection as one from water body. When an SNR threshold of 16v/v is used along

with an NDVI threshold of 0, the measurements are complementing each other to reduce the FPR significantly, while not introducing any substantial change in TPR. This threshold is also above the noise floor of L2 SNR measurements derived in [88]. This classification algorithm is then used to isolate windows of continuous reflections over water along a GNSS reflection track. Coherency analysis over the isolated windows is done, with more than 50% of the windows having a circular length of 0.97, showing highly coherent windows.

The thesis highlights the need to study such algorithms that can isolate windows of reflections over narrow water bodies on which coherency analysis can be done. Several other factors such as the effect of surface elevation of the observed area can be investigated to improve the accuracy of classifiers as one described in this thesis. This enables further research on altimetry applications on these windows where river flow can be calculated. These studies can also be extended towards monitoring the water body extent and mapping inundation. This can lead to the development of datasets for hydrologists for sustainable water resource management toward the fulfillment of the U.N. Sustainable Development Goals (SDGs).

Bibliography

[1] Copernicus Sentinel data [2021] for Sentinel data.

[2] U. S. Geological Survey, Canada Centre for Remote Sensing and Instituto Nacional de Estadística, Geografía e Informática (Mexico). (2004). Political Boundaries, North America USGS, Available at, 2004.

[3] Ndvi faqs: Frequently asked questions about the index, Jan 2023.

[4] Jonas Aeschbacher, Jiqing Wu, and Radu Timofte. In defense of shallow learned spectral reconstruction from rgb images. In Proceedings of the IEEE International Conference on Computer Vision Workshops, pages 471–479, 2017.

[5] Michal Aharon, Michael Elad, and Alfred Bruckstein. K-svd: An algorithm for designing overcomplete dictionaries for sparse representation. IEEE Transactions on signal processing, 54(11):4311–4322, 2006.

[6] Robert S Allison, Joshua M Johnston, Gregory Craig, and Sion Jennings. Airborne optical and thermal remote sensing for wildfire detection and monitoring. Sensors, 16(8):1310, 2016.

[7] Boaz Arad and Ohad Ben-Shahar. Sparse recovery of hyperspectral signal from natural rgb images. In European Conference on Computer Vision, pages 19–34. Springer, 2016.

[8] Boaz Arad, Ohad Ben-Shahar, and Radu Timofte. Ntire 2018 challenge on spectral reconstruction from rgb images. In Proceedings of the IEEE Conference on Computer Vision and Pattern Recognition Workshops, pages 929–938, 2018.

[9] Zoltan Bartalis, Wolfgang Wagner, Vahid Naeimi, Stefan Hasenauer, Klaus Scipal, Bonekamp Hans, J. Figa-saldaña, and Craig Anderson. Initial soil moisture retrievals from the metop-a advanced scatterometer (ascat). Geophysical Research Letters - GEOPHYS RES LETT, 34, 10 2007.

[10] Piotr Beckmann. The scattering of electromagnetic. Waves from Rough Surfaces, 1963.

[11] Swastik Bhattacharya, Kedar Remane, Bruce Kindel, and Gongguo Tang. Spectral super-resolution for hyperspectral image reconstruction using dictionary and machine learning. In IGARSS 2022 - 2022 IEEE International Geoscience and Remote Sensing Symposium, pages 1764–1767, 2022.

[12] Swastik Bhattacharya, Yang Wang, and Y. T. Jade Morton. Coherency statistics of discontinuously distributed windows of reflections over surface water detected using spire gnss-r grazing angle data. In 2023 IEEE Specialist Meeting on Reflectometry using GNSS and other Signals of Opportunity (GNSS+R), 2023. Accepted for Poster Presentation.

[13] Swastik Bhattacharya, Yang Wang, and Y. T. Jade Morton. Detection of surface water using spire grazing-angle gnss-r data. IEEE International Geoscience And Remote Sensing Symposium (IGARSS), 2023. Under review.

[14] Joseph W Boardman and Robert O Green. Exploring the spectral variability of the earth as measured by aviris in 1999. 2000.

[15] Leo Breiman. Random forests. Machine learning, 45(1):5–32, 2001.

[16] Adriano Camps, Hyuk Park, Enric Valencia i Domènech, Daniel Pascual, Francisco Martin, Antonio Rius, Serni Ribo, Javier Benito, Ana Andrés-Beivide, Paula Saameno, et al. Optimization and performance analysis of interferometric gnss-r altimeters: Application to the paris iod mission. IEEE Journal of Selected Topics in Applied Earth Observations and Remote Sensing, 7(5):1436–1451, 2014.

[17] Estel Cardellach, Antonio Rius, Manuel Martín-Neira, Fran Fabra, Oleguer Nogués-Correig, Serni Ribó, Juha Kainulainen, Adriano Camps, and Salvatore D'Addio. Consolidating the precision of interferometric gnss-r ocean altimetry using airborne experimental data. IEEE Transactions on Geoscience and Remote Sensing, 52(8):4992–5004, 2013.

[18] Gerardo A Carrillo-Niquete, José Luis Andrade, José René Valdez-Lazalde, Casandra Reyes-García, and José Luis Hernández-Stefanoni. Characterizing spatial and temporal deforestation and its effects on surface urban heat islands in a tropical city using landsat time series. Landscape and Urban Planning, 217:104280, 2022.

[19] Dudley B. Chelton, John C. Ries, Bruce J. Haines, Lee-Lueng Fu, and Philip S. Callahan. Chapter 1 satellite altimetry. In Lee-Lueng Fu and Anny Cazenave, editors, Satellite Altimetry and Earth Sciences, volume 69 of International Geophysics, pages 1–ii. Academic Press, 2001.

[20] Clara C Chew, Rashmi Shah, Cinzia Zuffada, and Anthony J Mannucci. Wetland mapping and measurement of flood inundated area using ground-reflected gnss signals in a bistatic radar system. In 2016 IEEE International Geoscience and Remote Sensing Symposium (IGARSS), pages 7184–7187. IEEE, 2016.

[21] MP Clarizia, CP Gommenginger, ST Gleason, MA Srokosz, C Galdi, and M Di Bisceglie. Analysis of gnss-r delay-doppler maps from the uk-dmc satellite over the ocean. Geophysical Research Letters, 36(2), 2009.

[22] Ian Collett, Yang Wang, Rashmi Shah, and Y. Jade Morton. Phase coherence of gps signal land reflections and its dependence on surface characteristics. IEEE Geoscience and Remote Sensing Letters, 19:1–5, 2022.

[23] Tanos Elfouhaily, Bertrand Chapron, Kristina Katsaros, and Douglas Vandemark. A unified directional spectrum for long and short wind-driven waves. Journal of Geophysical Research: Oceans, 102(C7):15781–15796, 1997.

[24] Tom Fawcett. An introduction to roc analysis. Pattern recognition letters, 27(8):861–874, 2006.

[25] Giuseppe Foti, Christine Gommenginger, Philip Jales, Martin Unwin, Andrew Shaw, Colette Robertson, and Josep Rosello. Spaceborne gnss reflectometry for ocean winds: First results from the uk techdemosat-1 mission. Geophysical Research Letters, 42(13):5435–5441, 2015.

[26] Silvano Galliani, Charis Lanaras, Dimitrios Marmanis, Emmanuel Baltsavias, and Konrad Schindler. Learned spectral super-resolution. arXiv preprint arXiv:1703.09470, 2017.

[27] James L Garrison, Justin K Voo, Simon H Yueh, Michael S Grant, Alexander G Fore, and Jennifer S Haase. Estimation of sea surface roughness effects in microwave radiometric measurements of salinity using reflected global navigation satellite system signals. IEEE Geoscience and Remote Sensing Letters, 8(6):1170–1174, 2011.

[28] Felipe Geremia-Nievinski, Matheus Ferreira e Silva, Karen Boniface, and Joao Francisco Galera Monico. Gps diffractive reflectometry: Footprint of a coherent radio reflection inferred from the sensitivity kernel of multipath snr. IEEE Journal of Selected Topics in Applied Earth Observations and Remote Sensing, 9(10):4884–4891, 2016.

[29] O Germain, Giulio Ruffini, F Soulat, M Caparrini, Bertrand Chapron, and P Silvestrin. The eddy experiment: Gnss-r speculometry for directional sea-roughness retrieval from low altitude aircraft. Geophysical research letters, 31(21), 2004.

[30] Utsav B Gewali, Sildomar T Monteiro, and Eli Saber. Spectral super-resolution with optimized bands. Remote Sensing, 11(14):1648, 2019.

[31] RR Gillies, WP Kustas, and KS Humes. A verification of the'triangle'method for obtaining surface soil water content and energy fluxes from remote measurements of the normalized difference vegetation index (ndvi) and surface e. International journal of remote sensing, 18(15):3145–3166, 1997.

[32] Scott Gleason. Towards sea ice remote sensing with space detected gps signals: Demonstration of technical feasibility and initial consistency check using low resolution sea ice information. Remote Sensing, 2(8):2017–2039, 2010.

[33] Scott Gleason, Mounir Adjrad, and Martin Unwin. Sensing ocean, ice and land reflected signals from space: results from the uk-dmc gps reflectometry experiment. In Proceedings of the 18th International Technical Meeting of the Satellite Division of The Institute of Navigation (ION GNSS 2005), pages 1679–1685, 2005.

[34] Scott Gleason, Stephen Hodgart, Yiping Sun, Christine Gommenginger, Stephen Mackin, Mounir Adjrad, and Martin Unwin. Detection and processing of bistatically reflected gps signals from low earth orbit for the purpose of ocean remote sensing. IEEE Transactions on Geoscience and Remote Sensing, 43(6):1229–1241, 2005.

[35] Noel Gorelick, Matt Hancher, Mike Dixon, Simon Ilyushchenko, David Thau, and Rebecca Moore. Google earth engine: Planetary-scale geospatial analysis for everyone. Remote Sensing of Environment, 2017.

[36] Michael S Grant, Scott T Acton, and Stephen J Katzberg. Terrain moisture classification using gps surface-reflected signals. IEEE Geoscience and Remote Sensing Letters, 4(1):41–45, 2007.

[37] Robert O Green, Michael L Eastwood, Charles M Sarture, Thomas G Chrien, Mikael Aronsson, Bruce J Chippendale, Jessica A Faust, Betina E Pavri, Christopher J Chovit, Manuel Solis, Martin R Olah, and Orlesa Williams. Imaging spectroscopy and the airborne visible/infrared imaging spectrometer (aviris). Remote Sensing of Environment, 65(3):227–248, 1998.

[38] HD GRIFFITHS. Advances in bistatic radar, 2007.

[39] Ravi P Gupta. Remote sensing geology. Springer, 2017.

[40] CD Hall and RA Cordey. Multistatic scatterometry. In International Geoscience and Remote Sensing Symposium,'Remote Sensing: Moving Toward the 21st Century'., volume 1, pages 561–562. IEEE, 1988.

[41] Martti T Hallikainen, Fawwaz T Ulaby, Myron C Dobson, Mohamed A El-Rayes, and Lil-Kun Wu. Microwave dielectric behavior of wet soil-part 1: Empirical models and experimental observations. IEEE Transactions on Geoscience and Remote Sensing, (1):25–34, 1985.

[42] Hans Hersbach, AD Stoffelen, and Sybren de Haan. An improved c-band scatterometer ocean geophysical model function: Cmod5. Journal of Geophysical Research: Oceans, 112(C3), 2007.

[43] Hristo D Hristov. Fresnal Zones in Wireless Links, Zone Plate Lenses and Antennas. Artech House, Inc., 2000.

[44] Hamza Issa, Georges Stienne, Serge Reboul, Mohamad Raad, and Ghaleb Faour. Airborne gnss reflectometry for water body detection. Remote Sensing, 14(1):163, 2021.

[45] Philip Jales, Stephan Esterhuizen, Dallas Masters, Vu Nguyen, Oleguer Nogués Correig, Takayuki Yuasa, and Jessica Cartwright. The new spire gnss-r satellite missions and products. In Image and Signal Processing for Remote Sensing XXVI, volume 11533, page 1153316. SPIE, 2020.

[46] Philip Jales, Stephan Esterhuizen, Dallas Masters, Vu Nguyen, Oleguer Nogués Correig, Takayuki Yuasa, and Jessica Cartwright. The new Spire GNSS-R satellite missions and products. In Lorenzo Bruzzone, Francesca Bovolo, and Emanuele Santi, editors, Image and Signal Processing for Remote Sensing XXVI, volume 11533, page 1153316. International Society for Optics and Photonics, SPIE, 2020.

[47] Katherine Jensen, Kyle McDonald, Erika Podest, Nereida Rodriguez-Alvarez, Viviana Horna, and Nicholas Steiner. Assessing l-band gnss-reflectometry and imaging radar for detecting sub-canopy inundation dynamics in a tropical wetlands complex. Remote Sensing, 10(9):1431, 2018.

[48] Stephen J Katzberg and Jason Dunion. Comparison of reflected gps wind speed retrievals with dropsondes in tropical cyclones. Geophysical Research Letters, 36(17), 2009.

[49] Stephen J Katzberg, Omar Torres, and George Ganoe. Calibration of reflected gps for tropical storm wind speed retrievals. Geophysical Research Letters, 33(18), 2006.

[50] A Kavak, WJ Vogel, et al. Using gps to measure ground complex permittivity. Electronics Letters, 34(3):254–255, 1998.

[51] Lawrence Klein and C Swift. An improved model for the dielectric constant of sea water at microwave frequencies. IEEE transactions on antennas and propagation, 25(1):104–111, 1977.

[52] Alaa Krayem, Ahmad Al Bitar, Ali Ahmad, Ghaleb Faour, Jean-Philippe Gastellu-Etchegorry, Issam Lakkis, Jocelyne Gerard, Haitham Zaraket, Aram Yeretzian, and Sara Najem. Urban energy modeling and calibration of a coastal mediterranean city: The case of beirut. Energy and Buildings, 199:223–234, 2019.

[53] J-P Lagouarde, Bimal K Bhattacharya, P Crébassol, P Gamet, Dheeraj Adlakha, CS Murthy, S Singh, Manoj Mishra, Rahul Nigam, PV Raju, et al. Indo-french high-resolution thermal infrared space mission for earth natural resources assessment and monitoring-concept and definition of trishna. In ISPRS-GEOGLAM-ISRS Joint International Workshop on "Earth Observations for Agricultural Monitoring", volume 42, page 403, 2019.

[54] Kristine M Larson, Johan S Löfgren, and Rüdiger Haas. Coastal sea level measurements using a single geodetic gps receiver. Advances in space research, 51(8):1301–1310, 2013.

[55] Kristine M Larson, Eric E Small, Ethan D Gutmann, Andria L Bilich, John J Braun, and Valery U Zavorotny. Use of gps receivers as a soil moisture network for water cycle studies. Geophysical Research Letters, 35(24), 2008.

[56] Zhongping Lee, Kendall L Carder, Curtis D Mobley, Robert G Steward, and Jennifer S Patch. Hyperspectral remote sensing for shallow waters. i. a semianalytical model. Applied optics, 37(27):6329–6338, 1998.

[57] Weiqiang Li, Estel Cardellach, Fran Fabra, Antonio Rius, Serni Ribó, and Manuel Martín-Neira. First spaceborne phase altimetry over sea ice using techdemosat-1 gnss-r signals. Geophysical Research Letters, 44(16):8369–8376, 2017.

[58] B Adams lJ John, Milton O Smith, and Alan R Gillespie. Simple models for complex natural surfaces: A strategy for the hyperspectral era of remote sensing. In IGARRS'S9, the IEEE International Geoscience and Remote Sensing symposium, 1989.

[59] Stephen T Lowe, Cinzia Zuffada, Yi Chao, Peter Kroger, Larry E Young, and John L LaBrecque. 5-cm-precision aircraft ocean altimetry using gps reflections. Geophysical Research Letters, 29(10):13–1, 2002.

[60] Manuel Martin-Neira et al. A passive reflectometry and interferometry system (paris): Application to ocean altimetry. ESA journal, 17(4):331–355, 1993.

[61] Y Jade Morton, Frank van Diggelen, James J Spilker Jr, Bradford W Parkinson, Sherman Lo, and Grace Gao. Position, navigation, and timing technologies in the 21st century: Integrated satellite navigation, sensor systems, and civil applications, volume 1. John Wiley & Sons, 2021.

[62] Samuel Munoz, Liviu Giosan, Matthew Therrell, Jonathan Remo, Zhixiong Shen, Richard Sullivan, Charlotte Wiman, Michelle O'Donnell, and Jeffrey Donnelly. Climatic control of mississippi river flood hazard amplified by river engineering. Nature, 556:95–98, 04 2018.

[63] Andrew O'Brien and Eric Loria. Overcoming the current limitations of gnss-r observation of wetlands and surface water. In 2021 IEEE International Geoscience and Remote Sensing Symposium IGARSS, pages 962–965. IEEE, 2021.

[64] Stephen E Palmer. Vision science: Photons to phenomenology. MIT press, 1999.

[65] Gintautas Palubinskas, Franz Kurz, and Peter Reinartz. Detection of traffic congestion in optical remote sensing imagery. In IGARSS 2008-2008 IEEE International Geoscience and Remote Sensing Symposium, volume 2, pages II–426. IEEE, 2008.

[66] Jean-François Pekel, Andrew Cottam, Noel Gorelick, and Alan S Belward. High-resolution mapping of global surface water and its long-term changes. Nature, 540(7633):418–422, 2016.

[67] Nathalie Pettorelli. The normalized difference vegetation index. Oxford University Press, 2013.

[68] Saurabh Prasad, Lori M Bruce, and Jocelyn Chanussot. Optical remote sensing. Advances in Signal Processing and Exploitation Techniques, 2011.

[69] Antonio Rius, Oleguer Nogués-Correig, Serni Ribó, Estel Cardellach, Santi Oliveras, Enric Valencia, Hyuk Park, José Miguel Tarongí, Adriano Camps, Hans van der Marel, et al. Altimetry with gnss-r interferometry: First proof of concept experiment. GPS solutions, 16:231–241, 2012.

[70] Nereida Rodriguez-Alvarez, Adriano Camps, Mercè Vall-Llossera, Xavier Bosch-Lluis, Alessandra Monerris, Isaac Ramos-Perez, Enric Valencia, Juan Fernando Marchan-Hernandez, Jose Martinez-Fernandez, Guido Baroncini-Turricchia, et al. Land geophysical parameters retrieval using the interference pattern gnss-r technique. IEEE Transactions on Geoscience and Remote Sensing, 49(1):71–84, 2010.

[71] Carolyn J Roesler, Y Jade Morton, Yang Wang, and R Steven Nerem. Coherent gnss-reflections characterization over ocean and sea ice based on spire global cubesat data. IEEE Transactions on Geoscience and Remote Sensing, 60:1–18, 2021.

[72] C Ruf, M Unwin, J Dickinson, R Rose, D Rose, M Vincent, and A Lyons. Cygnss: Enabling the future of hurricane prediction [remote sensing satellites]. IEEE Geoscience and Remote Sensing Magazine, 1(2):52–67, 2013.

[73] Christopher Ruf, Scott Gleason, Aaron Ridley, Randall Rose, and John Scherrer. The nasa cygnss mission: Overview and status update. In 2017 IEEE International Geoscience and Remote Sensing Symposium (IGARSS), pages 2641–2643. IEEE, 2017.

[74] G. Schaepman-Strub, M.E. Schaepman, T.H. Painter, S. Dangel, and J.V. Martonchik. Reflectance quantities in optical remote sensing—definitions and case studies. Remote Sensing of Environment, 103(1):27–42, 2006.

[75] Michael Schmitt. Potential of large-scale inland water body mapping from sentinel-1/2 data on the example of bavaria's lakes and rivers. PFG–Journal of Photogrammetry, Remote Sensing and Geoinformation Science, 88(3):271–289, 2020.

[76] AM Semmling, Georg Beyerle, Ralf Stosius, Galina Dick, Jens Wickert, F Fabra, Estel Cardellach, Serni Ribó, A Rius, Achim Helm, et al. Detection of arctic ocean tides using interferometric gnss-r signals. Geophysical Research Letters, 38(4), 2011.

[77] José Antonio Sobrino and N Raissouni. Toward remote sensing methods for land cover dynamic monitoring: Application to morocco. International journal of remote sensing, 21(2):353–366, 2000.

[78] David R Thompson, KN Babu, Amy J Braverman, Michael L Eastwood, Robert O Green, Jonathan M Hobbs, Jeffrey B Jewell, Bruce Kindel, Steven Massie, Manoj Mishra, et al. Optimal estimation of spectral surface reflectance in challenging atmospheres. Remote Sensing of Environment, 232:111258, 2019.

[79] Radu Timofte, Vincent De Smet, and Luc Van Gool. A+: Adjusted anchored neighborhood regression for fast super-resolution. In Asian conference on computer vision, pages 111–126. Springer, 2014.

[80] P.A. Townsend, J.R. Foster, R.A. Chastain, and W.S. Currie. Application of imaging spectroscopy to mapping canopy nitrogen in the forests of the central appalachian mountains using hyperion and aviris. IEEE Transactions on Geoscience and Remote Sensing, 41(6):1347–1354, 2003.

[81] Joel A Tropp and Anna C Gilbert. Signal recovery from random measurements via orthogonal matching pursuit. IEEE Transactions on information theory, 53(12):4655–4666, 2007.

[82] Susan L Ustin, Dar A Roberts, John A Gamon, Gregory P Asner, and Robert O Green. Using imaging spectroscopy to study ecosystem processes and properties. BioScience, 54(6):523–534, 2004.

[83] Swapnil S Vyas and Bimal K Bhattacharya. Agricultural drought early warning from geostationary meteorological satellites: concept and demonstration over semi-arid tract in india. Environmental Monitoring and Assessment, 192:1–15, 2020.

[84] Yang Wang and Y Jade Morton. River slope observation from spaceborne gnss-r carrier phase measurements: a case study. IEEE Geoscience and Remote Sensing Letters, 19:1–5, 2021.

[85] Yang Wang and Y. Jade Morton. River slope observation from spaceborne gnss-r carrier phase measurements: A case study. IEEE Geoscience and Remote Sensing Letters, 19:1–5, 2022.

[86] Jean-Pierre Wigneron, Thomas Schmugge, André Chanzy, Jean-Claude Calvet, and Yann H Kerr. Use of passive microwave remote sensing to monitor soil moisture. Agronomie, 18(1):27–43, 1998.

[87] Valery U Zavorotny, Kristine M Larson, John J Braun, Eric E Small, Ethan D Gutmann, and Andria L Bilich. A physical model for gps multipath caused by land reflections: Toward bare soil moisture retrievals. IEEE Journal of Selected Topics in Applied Earth Observations and Remote Sensing, 3(1):100–110, 2009.

[88] Jiahua Zhang, Y. Jade Morton, Yang Wang, and Carolyn J. Roesler. Mapping surface water extents using high-rate coherent spaceborne gnss-r measurements. IEEE Transactions on Geoscience and Remote Sensing, 60:1–15, 2022.

Appendix A

K-Singular Value Decomposition

K-Singular Value Decomposition (K-SVD) is a dictionary learning algorithm demonstrated in [5] to train an overcomplete dictionary. The algorithm begins with an initial guess of the dictionary $\mathbf{\Phi}^*$, which is an $N \times P$ matrix. The dictionary is defined as:

$$\mathbf{\Phi}^* = \begin{bmatrix} \phi_1 & \phi_2 & \dots & \phi_P \end{bmatrix} \tag{A.1}$$

The dictionary provides a sparse representation of the signals in a training set, represented as an $N \times L$ matrix:

$$F = \begin{bmatrix} f_1 & f_2 & \dots & f_L \end{bmatrix} \tag{A.2}$$

The transform coefficients can be represented as a $P \times L$ matrix A, such that;

$$A = \begin{bmatrix} a_1 & a_2 & \dots & a_L \end{bmatrix} \tag{A.3}$$

and,

$$||F - \mathbf{\Phi}^* A||_F^2 = \sum_{l=1}^{L} ||f_l - \mathbf{\Phi}^* a_l||_2^2 \tag{A.4}$$

The coefficient vectors are sparse:

$$||a_l||_0 \leq M \tag{A.5}$$

Post initialization, the algorithm alternates between two stages:

(1) *Sparse Coding:* In this stage, the current guess of the dictionary $\mathbf{\Phi}^*$ is fixed, and coefficients in A are updated. It is intended to minimize $||f_l - \mathbf{\Phi}^* a_l||_2^2$ subject to $||a_l||_0 \leq M$ for all $l = 0, 1, \ldots, L$. This can be achieved through an algorithm such as Orthogonal Matching Pursuit (OMP).

(2) *Dictionary Learning Stage:* In this stage, the dictionary atoms are updated one at a time. The associated non-zero coefficients in A are updated as well, accelerating convergence.

For each $p = 1, 2, \ldots, P$, the atoms ϕ_p are updated as follows:

- Identify signals that use this atom:

$$\omega_p := \{l : a_l(p) \neq 0\}$$

- Let the rows of the matrix A be denoted by $a^1, a^2, \ldots, a^P$. It is to be noted that:

$$||F - \mathbf{\Phi}^* A||_F^2 = ||F - \sum_{k=1}^{P} \phi_k a^k||_F^2$$

  Now, a matrix E_p is the residual training error when the p_{th} atom is removed. The matrix E_p^R is the restriction to E_p when the columns corresponding to ω_p is removed.

- Compute the SVD of E_p^R : $E_p^R = U \Sigma V^*$. Choose the updated dictionary element ϕ_p to be the first column of U. On the indices of ω_p, update the coefficient vector a^p by multiplying $\Sigma(1,1)$ times the first column of V.

Appendix B

Coherency Detection algorithm using Phase Noise

This appendix presents an algorithm to detect coherency in reflections as demonstrated in [71]. This algorithm requires the reflected path phase measurements (ϕ_r), SNR measurements (in v/v) and noise fraction N_{frac} for the band of frequency measurement used. It is to be noted that the measurements are taken at a rate of 50Hz, or 0.02 seconds. It is denoted by the variable *rate*. The coherency is determined with the following steps:

- Extract reflected path carrier phase, SNR measurements, and noise fraction.
- With the help of noise fraction, calculate amplitude of I (In-phase) and Q (quadrature) measurements as:

$$A = \frac{SNR \times N_{frac}}{\sqrt{rate}} \tag{B.1}$$

- The I and Q measurements are calculated as:

$$I = Acos(\phi_r) \tag{B.2}$$

$$Q = Asin(\phi_r) \tag{B.3}$$

- Smooth the calculated I and Q measurements using a 5-sample averaging filter.
- Calculate the denoised phase measurements ϕ_{r5} using the smoothed I and Q and calculate the phase noise $\Delta\phi$ measurements as:

$$\phi_{r5} = arctan2(Q_{smooth}, I_{smooth}) \tag{B.4}$$

$$\Delta\phi = \phi_r - \phi_{r5} \tag{B.5}$$

- Convert the $\Delta\phi$ measurements from radians to degrees, such that their values are between -180^o and 180^o.
- Split the measurements into different time windows. In this thesis, the minimum window length is 5, and maximum is 15.
- For each time window, calculate the 80^{th} percentile of the SNR measurements (SNR_{80}).
- For each time window, calculate the circular length (c_{len}) [**?**] and circular kurtosis (c_{kur}) [**?**] of the measurements $\Delta\phi$.
- If $c_{len} \geq -1.15(c_{kur} - 0.75) + 0.8$ and $SNR_{80} > 15$, then the reflections in the window are coherent. In case when $c_{len} < -1.15(c_{kur} - 0.75) + 0.8$ and $c_{len} \geq -1.15(c_{kur} - 0.6) + 0.43$ and $SNR_{80} > 15$, the reflections in the window are semi-coherent. In all other cases, the reflections are incoherent.